

ALMA MATER STUDIORUM  
UNIVERSITÀ DI BOLOGNA  
SEDE DI CESENA

---

Scuola di Ingegneria ed Architettura  
Corso di Laurea in Ingegneria Elettronica e Telecomunicazioni per  
l'Energia

# PERFORMANCE ANALYSIS OF A RADAR SYSTEM BASED ON 5G SIGNALS

Elaborato in  
Reti Wireless per l'Internet of Things

*Tesi di Laurea di:*  
ELISABETTA MATRICARDI

*Relatore:*  
Prof. Ing.  
ENRICO PAOLINI

*Correlatori:*  
Prof. Ing.  
ANDREA GIORGETTI  
Dott. Ing.  
LORENZO PUCCI

---

SESSIONE III  
ANNO ACCADEMICO 2019-2020



## **KEYWORDS**

OFDM Radar

5G Signal

Periodogram

Detection

Estimation Theory



# Acronyms

**3G** third generation

**3GPP** third generation partnership project

**4G** fourth generation

**5G** fifth generation

**ADC** analog-to-digital converter

**AWGN** additive white Gaussian noise

**CE** cyclic extension

**CP** cyclic prefix

**CP-OFDM** cyclic prefix orthogonal frequency division multiplexing

**CRB** common resource block

**CSI** channel state information

**DAC** digital-to-analog converter

**DC** direct current

**DFT** discrete Fourier transform

**DL** downlink

**DTFT** discrete time Fourier Transform

**ELP** equivalent low-pass

**FDD** frequency division duplex

**FFT** fast Fourier transform

**ICI** intercarrier interference

**IDFT** inverse discrete Fourier transform

**IFFT** inverse fast Fourier transform

**ISI** inter-symbol interference

**JCR** joint communication and radar

**LOS** line-of-sight

**LTE** long term evolution

**MIMO** multiple-input-multiple-output

**NLOS** non-line-of-sight

**NR** new radio

**OFDM** orthogonal frequency division multiplexing

**PAPR** peak to average power ratio

**PBCH** physical broadcast channel

**PDCCH** physical downlink control channel

**PRB** physical resource block

**PSD** power spectral density

**PSK** phase-shift keying

**QAM** quadrature amplitude modulation

**QPSK** quadrature phase-shift keying

**RB** resource block

**RC** raised cosine

**RCS** radar cross section

**RE** resource element

**RF** radio frequency

**RMSE** root mean square error

---

**ROC** receiver operating characteristic

**SCS** subcarrier spacing

**SIR** signal to interference ratio

**SNR** signal to noise ratio

**TDD** time division duplex

**UL** uplink

---



# Abstract

Since spectrum is becoming a more and more scarce resource, the idea of reusing it for more than one application is attractive, as it can avoid under-utilization of otherwise permanently allocated spectral resources. Over the past few years, an alternative to radar signals has been studied, which consists of digitally generated orthogonal frequency division multiplexing (OFDM) waveforms.

This thesis aims to investigate the performance of a communication signal, the fifth generation (5G) new radio (NR) one, when used for sensing purposes. A radar system and a processing algorithm based on frequency domain OFDM radar processing are implemented and complemented with an interpolation method to account for null subcarriers within the transmit resource grid. Then, computer simulations are performed to evaluate range and velocity estimation performance; it is shown that low target estimation error can be achieved even at low signal to noise ratio (SNR). Furthermore, 5G NR waveforms, thanks to their impressive channel bandwidth, scalable numerology and robustness against multipath, are proved to perform well even in fading channels. Through the help of receiver operating characteristic (ROC) curves, the difference of the radar performance is illustrated when two types of radio channels are used, which are the additive white Gaussian noise (AWGN) and multipath fading channel.



# Contents

<b>Introduction</b>	<b>1</b>
<b>1 OFDM System</b>	<b>3</b>
1.1 OFDM Signal Generation . . . . .	3
1.2 Guard Time and Cyclic Extension . . . . .	6
1.3 Oversampling . . . . .	9
1.4 OFDM Radar Principle . . . . .	11
1.4.1 High Peak-to-Average Power Ratio (PAPR) . . . . .	12
<b>2 5G New Radio Physical Layer</b>	<b>15</b>
2.1 5G Use Cases . . . . .	15
2.2 5G Spectrum . . . . .	16
2.3 Frame Structure and Numerology . . . . .	17
2.3.1 Time Domain Structure . . . . .	19
2.3.2 Frequency Domain Structure . . . . .	20
2.3.3 Bandwidth Part . . . . .	22
2.3.4 Transmission Techniques . . . . .	23
<b>3 OFDM Radar</b>	<b>25</b>
3.1 OFDM Radar Estimation Problem . . . . .	25
3.1.1 Interpolation . . . . .	29
3.2 Periodogram-based Estimation Algorithms . . . . .	29
3.2.1 Distance Estimation Parameters . . . . .	31
3.2.2 Velocity Estimation Parameters . . . . .	33
3.2.3 OFDM Radar Parametrization . . . . .	33
3.2.4 Signal-to-Noise Ratio and Processing Gain . . . . .	34
3.2.5 Window Functions . . . . .	35
<b>4 5G NR Performance Results</b>	<b>39</b>
4.1 Range-Doppler Image . . . . .	40
4.2 Performance in AWGN Channel . . . . .	42

---

4.2.1	Numerical Performance Analysis . . . . .	43
4.3	Performance in Multipath Fading Channel . . . . .	45
4.3.1	Channel Characterization . . . . .	45
4.3.2	Numerical Results . . . . .	47
4.4	Signal Detection and False Alarm Rate . . . . .	52
<b>Conclusions</b>		<b>59</b>
<b>List of Figures</b>		<b>62</b>
<b>Bibliography</b>		<b>63</b>

---

# Introduction

Given the abundance of connected devices and services, the frequency spectrum is becoming increasingly congested with the rapid growth of the wireless communication industry. With the allocation of the available frequency bands to wireless communication systems such as 5G NR, long term evolution (LTE) and Wi-Fi, the interference in the radar bands is on the rise and has raised concerns both from government and military organizations for the safeguard of critical radar operations. To this end, research efforts are well underway to address the issue of sharing communications and radar spectrum [1]. Over the past few years, a possible alternative has been studied, capable of achieving performance beyond the conventional radar systems operating with analog-generated linear frequency modulated signals. This alternative consists of a radar operating with digitally generated OFDM waveforms.

Due to the wide use of OFDM for various communication applications, and thanks to the robustness against multipath fading and high flexibility in radio resource management, many researches have been focused on combining OFDM radar with communication in order to jointly perform sensing and communication, motivated by the efficient use of limited spectral resources based on a single waveform capable of performing both applications.

Therefore, this work aims to study the feasibility of a radar operating with digital generated OFDM waveforms with particular focus on the 5G NR mobile networks' base station and their utilization for radar purposes [13].

This thesis is organized as follows:

- In Chapter 1 a description of a general OFDM system and signal structure is proposed, with emphasis on the cyclic prefix and its advantages both in communications and radar sensing.
- Chapter 2 provides an overview of the 5G signal, focusing on the parameters necessary from a radar sensing point of view, such as the subcarrier spacing, the channel bandwidth and the resource grid. A detailed description of the different numerologies introduced for the 5G physical layer and of the radio frame structure, both in the time

and frequency domain, is given.

- Chapter 3 presents a classical signal processing model for a basic monostatic OFDM radar system and a signal processing algorithm for distance and velocity estimation based on frequency-domain processing.
  - Chapter 4 shows the main performance results of the OFDM radar algorithm applied to the 5G signal. At first the correctness of the detection algorithm is proved and then the performance is analyzed when two different kinds of channels are considered.
-

# Chapter 1

## OFDM System

During the development phase of the 5G technology, many waveforms and modulation techniques were taken into consideration, but cyclic prefix orthogonal frequency division multiplexing (CP-OFDM) was chosen as the main candidate.

The OFDM is a frequency multiplexing technique based on transmission of multiple parallel data streams on orthogonal frequency subcarriers, used when a high data rate traffic is transmitted over a frequency-selective radio channel. The OFDM transmission technique allows to split the total available bandwidth BW into many narrow subchannels with low data-rate, spaced on the frequency axis by a factor  $\Delta f$ . The channels can be made narrow enough to consider a flat channel spectral response, allowing single tap equalization. Each subchannel is modulated individually and transmitted simultaneously in a parallel form.

### 1.1 OFDM Signal Generation

The OFDM signal is made up of a sum of  $N$  complex orthogonal subcarriers (indexed with  $k = \{0, 1, 2, \dots, N - 1\}$ ), each one independently modulated. The input bits are mapped into the complex symbols  $d_k[n]$  usually following an M-QAM modulation (or M-PSK modulation).

One OFDM symbol with duration  $T$  and starting at  $t = t_s$  has the following passband expression in the time domain, referred to the carrier frequency  $f_c$  [2].

$$s_k(t) = \begin{cases} [h] \operatorname{Re} \left\{ \sum_{k=0}^{N-1} d_k e^{j2\pi \left( f_c + \frac{(N-1-2k)}{2T} (t-t_s) \right)} \right\}; & t \in [t_s, t_s + T] \\ 0 & ; \quad \textit{otherwise.} \end{cases} \quad (1.1)$$

Figure 1.1 shows a representation of a general OFDM system. In this system, the M-QAM modulated symbols are critically sampled (one sample per information symbol/subcarrier) at a rate  $f_s = 1/T_d$ , where  $T_d$  is the duration of the symbol at the output of the M-QAM modulator, grouped within the vector  $\mathbf{d}_x = [d_x[0], \dots, d_x[N-1]]^T$  of length  $N$ . The symbols  $d_x[n]$  are parallelized and fed to the inverse fast Fourier transform (IFFT) to modulate separately the  $N$  orthogonal subcarriers during the whole  $i$ -th time interval  $I_i = [iT, iT + T]$ , defined for one OFDM symbol with period  $T = NT_d = N/f_s$ . After serialization, the output represents the digital OFDM signal in time domain. For any instant  $t$  the complex envelope of the base-band OFDM signal can be written as:

$$b_x(t) = \sum_{k=0}^{N-1} d_x(k, i) e^{j2\pi f_k t}; \quad t \in I_i \quad (1.2)$$

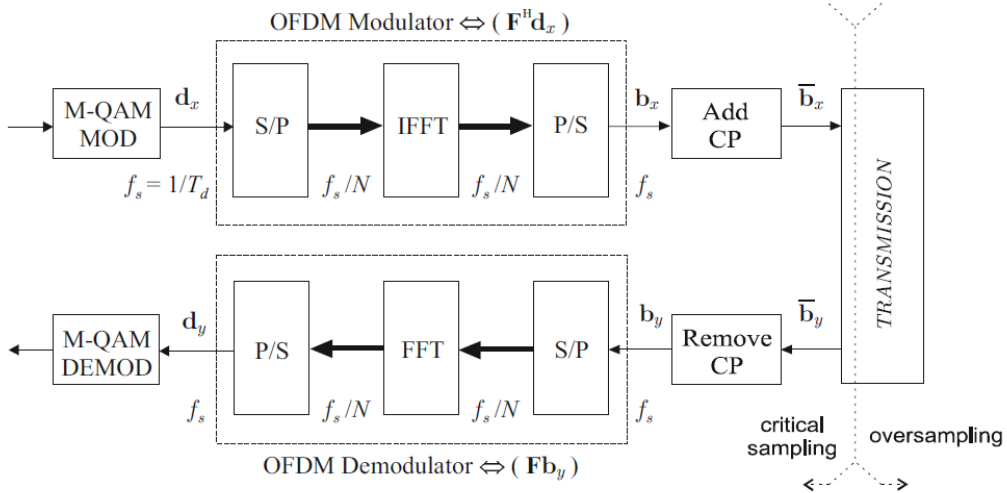


Figure 1.1: Block diagram of the OFDM modulation stages [2].

where  $f_k = \frac{kf_s}{N} = \frac{k}{T}$  is the  $k$ -th subcarrier frequency and  $d_x(k, i)$  is the M-QAM symbol modulating the  $k$ -th carrier during the whole  $i$ -th OFDM symbol interval [3].

From (1.2), the corresponding OFDM symbol at the critical sampling rate  $f_s$  consists of a set of  $T_d$ -spaced base-band signal samples  $\mathbf{b}_x = [b_x[0], b_x[1], \dots, b_x[N-1]]^T$ . At the transmitter, this enables efficient generation of digital OFDM signals by taking the inverse discrete Fourier transform (IDFT) of the incoming data-frame  $\mathbf{d}_x$ . Therefore, the  $n$ -th element of the equivalent low-pass (ELP) signal  $b_x(t)$  is given by:

$$\begin{aligned}
b_x[n] = b_x(nT_d) &= \sum_{k=0}^{N-1} d_x[k] e^{j\frac{2\pi}{N}nk} w[n/(N-1)] \\
&= N \cdot \text{IDFT}[d_x[k]] = N \cdot \text{IFFT}[d_x[k]]
\end{aligned} \tag{1.3}$$

where  $w[\cdot]$  is a discrete rectangular window that is defined by

$$w[r] = \begin{cases} [h] & 1 & ; & 0 \leq r \leq 1 \\ & 0 & ; & \textit{otherwise.} \end{cases} \tag{1.4}$$

The calculation of (1.3) for  $(n, k) = \{0, \dots, N-1\}$  can be equivalently performed as the following matrix operation:

$$\mathbf{b}_x = \mathbf{F}^H \mathbf{d}_x \tag{1.5}$$

where  $\mathbf{F}$  is the discrete Fourier transform (DFT) matrix whose hermitian is associated to the inverse operation IDFT. According to (1.5) and (1.3) this matrix  $\mathbf{F}$  can be defined as:

$$\mathbf{F}_{(N \times N)} = \begin{bmatrix} 1 & 1 & 1 & 1 & \dots & 1 \\ 1 & e^{-j\frac{2\pi}{N}} & e^{-j\frac{4\pi}{N}} & e^{-j\frac{6\pi}{N}} & \dots & e^{-j2\pi\frac{N-1}{N}} \\ 1 & e^{-j\frac{4\pi}{N}} & e^{-j\frac{8\pi}{N}} & e^{-j\frac{12\pi}{N}} & \dots & e^{-j4\pi\frac{N-1}{N}} \\ 1 & e^{-j\frac{6\pi}{N}} & e^{-j\frac{12\pi}{N}} & e^{-j\frac{18\pi}{N}} & \dots & e^{-j6\pi\frac{N-1}{N}} \\ \vdots & \vdots & \vdots & \vdots & \ddots & \vdots \\ 1 & e^{-j2\pi\frac{N-1}{N}} & e^{-j4\pi\frac{N-1}{N}} & e^{-j6\pi\frac{N-1}{N}} & \dots & e^{-j2\pi\frac{(N-1)^2}{N}} \end{bmatrix} \tag{1.6}$$

where this important condition can be observed:

$$\mathbf{F}^H \mathbf{F} = \mathbf{I}_{(N)}. \tag{1.7}$$

Every column in (1.6) corresponds to a complex subcarrier with a normalized frequency that depends on the size of the Fourier Transform ( $N$  must be power of 2 in order to perform IFFT and fast Fourier transform (FFT) using a radix-2 or radix-4 algorithm).

After the IFFT is performed and the signal is reconverted from parallel to serial, a cyclic prefix (CP), which will be better discussed later, is appended to the OFDM symbol to avoid inter-symbol interference (ISI) at the receiver. Subsequently, the resulting signal is converted to the analog domain with a digital-to-analog converter (DAC) and then is transmitted through the channel.

---

At the receiver, the signals are analogously quadrature demodulated, sampled with analog-to-digital converters (ADCs) after which the CP is removed. To simplify the basic signal model description it is assumed that the transmission block is characterized by a perfectly linear discrete transfer function. Then, according to this assumption, for signals sampled at the Nyquist rate, the OFDM demodulation consists of applying an FFT to the transmitted ELP signal samples  $b_y[m]$  to recover the original M-QAM data. Hence, the  $k$ -th data symbol given to the M-QAM demodulator is obtained as follows:

$$d_y[k] = \sum_{m=0}^{N-1} b_y[m] e^{-j \frac{2\pi}{N} mk}. \quad (1.8)$$

At the receiver, the vector  $\mathbf{d}_y = [d_y[0], \dots, d_y[N-1]]^T$ , with the demodulated M-QAM symbols from the respective transmitted block, can also be obtained by multiplying the received sequence  $\mathbf{b}_y$  by the matrix  $\mathbf{F}$  in (1.6):

$$\mathbf{d}_y = \mathbf{F} \mathbf{b}_y. \quad (1.9)$$

## 1.2 Guard Time and Cyclic Extension

One of the benefits of the OFDM transmission technique is its effective way of dealing with the spread of multipath delay. To prevent ISI, such that different symbols do not overlap at the receiver despite different delays of the multipath channel, a guard interval is inserted between OFDM base-band signal blocks. Typically, this guard time is greater than the predicted delay spread, so that multipath components from one symbol do not interfere with the next one. The guard time could consist of no signal at all. However, this solution would allow to solve the ISI problem, but at the same time, it would lead to the intercarrier interference (ICI) problem. In fact, by adding a number of zeros in the guard time, the subcarriers could lose their orthogonality because there could be a non-integer number of cycles within the FFT interval.

To overcome the ICI problem, normally the OFDM is cyclically extended along the guard time, so that any subcarrier coming from direct or delayed signal replicas will continue to have an integer number of cycles within an FFT period, as long as the delay is smaller than the guard time. In Figure 1.2 this cyclic extension (CE) is implemented by copying the last  $N_{\text{CE}}$  samples of the IFFT-block output, of length  $N$ , at the start of the OFDM symbol. So, the total symbol duration becomes equal to  $T_1 = T + T_{\text{CE}}$  adding the last  $N_{\text{CE}}$  samples, of the original signal vector of length  $N$ , to the front of

---

the extended symbol, thus forming the cyclic prefix  $N_{\text{CE}}$ .

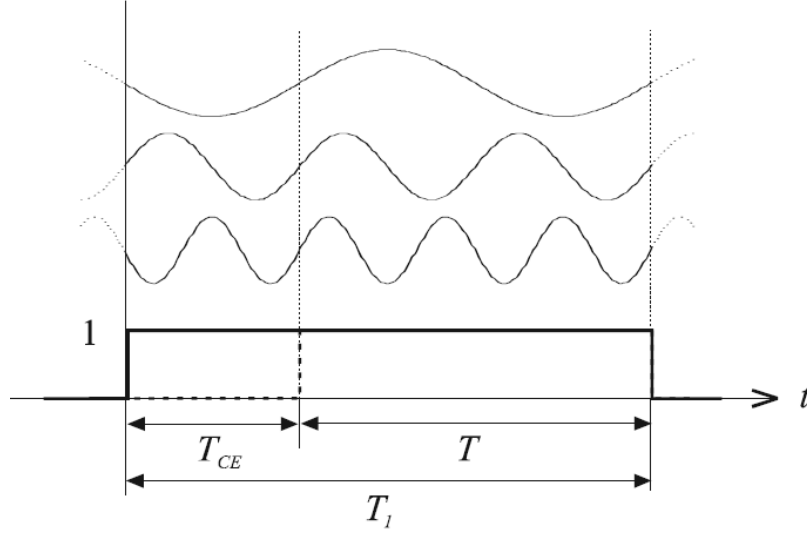


Figure 1.2: Cyclic extension and windowing for three OFDM subcarriers [2].

As already stated, the guard time must be chosen larger than the maximum duration of impulse response among the  $N$  subchannels. As long as the frequency spectrum is concerned, this means that the ICI in OFDM is avoided since the maximum of any single subcarrier should correspond to the zero crossing of all the other subcarriers.

Hereafter,  $\bar{x}$  will represent the cyclically extended version of any discrete signal  $x$ , and  $N_{\text{CE}}$  the length of CP, as a number of samples. Furthermore, at critical sampling rate will have  $T_1 = T \frac{N_{\text{CE}}}{N}$ .

The samples of the cyclically extended OFDM symbol in discrete-time are described from (1.3) by including a simple extension of the discrete window  $w[\cdot]$ ,

$$\bar{b}_x[n] = \sum_{k=0}^{N-1} d_x[k] e^{j \frac{2\pi}{N} nk} w[n / (N + N_{\text{CE}}) - 1]. \quad (1.10)$$

The CE operation over the input vector  $\mathbf{b}_x$  can be defined as:

$$\bar{\mathbf{b}}_x = \mathbf{P}_\eta \mathbf{b}_x \quad (1.11)$$

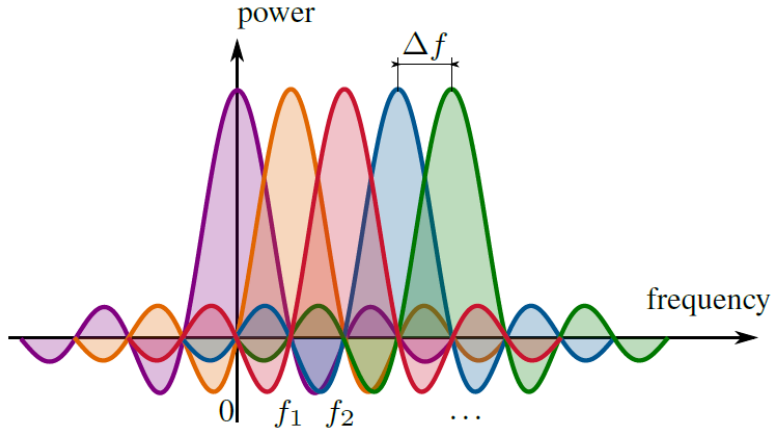


Figure 1.3: Spectrum of an OFDM signal [5].

where the cyclic extension operator  $\mathbf{P}_\eta$  depends on the relation  $\eta = \frac{N_{\text{CE}}}{N}$  which defines the following partitioned matrix:

$$\mathbf{P}_\eta = \begin{bmatrix} \mathbf{0}_{(N_{\text{CE}} \times N_\Delta)} & \mathbf{I}_{(N_{\text{CE}})} \\ \mathbf{I}_{(N)} \end{bmatrix} \quad (1.12)$$

where  $N > N_{\text{CE}}$  and  $N_\Delta = N - N_{\text{CE}}$ . Hence, in (1.11) this matrix adds the last  $N_{\text{CE}}$  samples of the original signal vector of length  $N$  at the start of the OFDM symbol, thus forming the cyclic prefix  $N_{\text{CE}}$ . In general, the dimensions of  $\mathbf{P}_\eta$  depend on the length of the vector to be extended. This will depend on whether the CE process takes place before or after signal oversampling, which will be discussed in the next section.

The definition of one independent OFDM symbol implies that the subcarriers should be declared null when out of the corresponding interval of duration  $T$ . Nevertheless, in practice the system will transmit the cyclically extended symbol  $\bar{\mathbf{b}}_x$  where these  $N$  components are no longer orthogonal, although they remain centered at the same frequencies  $f_k$ . Therefore, in the reception branch, the samples of the CE must be discarded to re-create the original OFDM symbol, thus obtaining the periodic-like signal block. Furthermore,

windowing the received frame by  $T$  is required to restore the orthogonality between subcarriers before demodulation. Nevertheless, removing the CE (along with the use of guard time which is discussed later) implies a certain cost in terms of SNR. Thus, processing the CE leads to a better spectral efficiency but at the cost of increasing processing complexity.

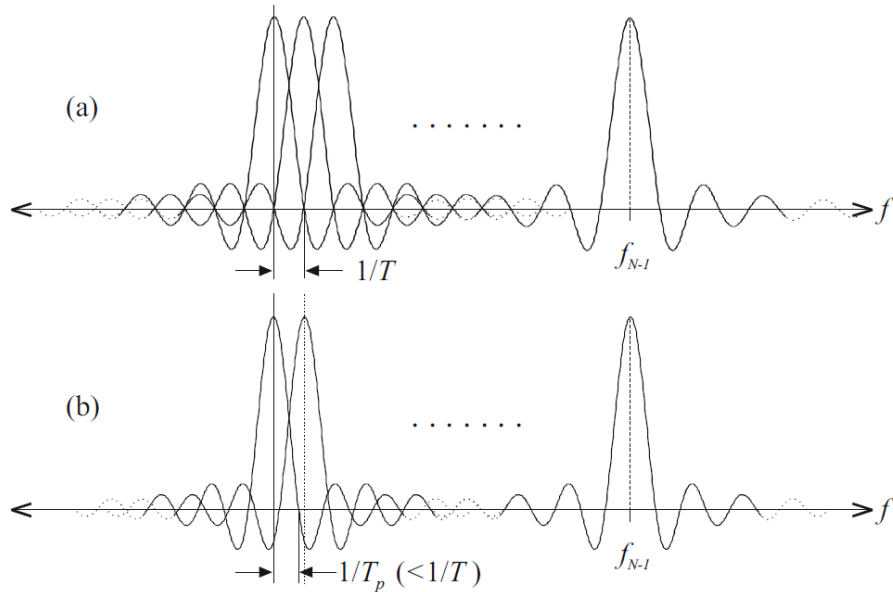


Figure 1.4: Comparison between OFDM spectra using two different values for the window that defines the FFT interval. (a) using  $T_p=T$  results in orthogonality, (b) using  $T_p > T$  the subcarriers are no longer orthogonal [2].

### 1.3 Oversampling

In previous expressions, the indexing of the elements from time-dependent vectors and the discrete-time evaluation using  $(nT_s) = [n]$  coincide in denoting the critical sampling at Nyquist rate. However, since oversampling should take place according to transmission hardware requirements, another notation must be introduced, such as  $\mathbf{x}[n/L]$ , to refer in general to the oversampling of the signal  $\mathbf{x}[n]$  by a factor  $L$ , and  $\mathbf{x}_L$  for the oversampled version of any vector  $\mathbf{x}$  [2].

In fact, if oversampling was not present, when the samples of the OFDM symbol pass through a DAC converter intolerable aliasing would be intro-

duced, due to the critical sampling chosen. The time-domain interpolation typically consists of two steps: the addition of  $(L - 1)$  zeros in the original sequence after each sample, and then a lowpass filtering of the resulting extended sequence resulting from it. The vector at the output of the interpolator filter then includes the unmodified original samples with  $(L - 1)$  interpolated values in between. The first half of the rows in the complex IFFT corresponds to positive frequencies while the second half corresponds to negative frequencies. The zeros can then be inserted at the center of the data vector when oversampling is used so that the zero data value is assigned to frequencies close to  $\pm \frac{f_s}{2}$ , while the nonzero data values are mapped onto subcarriers around 0 Hz. Regardless of the cyclical extension, it is assumed that the spectrum of a well interpolated sequence  $\mathbf{b}_{xL}$  is almost identical to the spectrum that would result from sampling the original signal  $\mathbf{b}_x$  at an  $L$ -times higher sampling rate. In practice, an oversampled version of (1.3) can be obtained more efficiently through a frequency-domain interpolation, which can be implemented by zero padding the IFFT as shown in Figure 1.5 [2]:

$$\begin{aligned}
 b_{x[\frac{n}{L}]} &= \sum_{k=0}^{N-1} d_x[k] e^{j \frac{2\pi}{NL} nk} w[n/(NL - 1)] \\
 &= \left( \sum_{k=0}^{\frac{N}{2}-1} d_x[k] e^{j \frac{2\pi}{NL} nk} + \sum_{k=NL-\frac{N}{2}}^{NL-1} d_x[k - N(L - 1)] e^{j \frac{2\pi}{NL} nk} \right) w[n/(NL - 1)] \\
 &= NL \cdot \text{IDFT}[d_x[0] \dots d_x[N/2 - 1] \underbrace{0 \dots 0}_{N(L-1)} d_x[N/2] \dots d_x[N - 1]] \\
 &= NL \cdot \text{IDFT}[d_{x_{zp}}].
 \end{aligned} \tag{1.13}$$

Thus, the oversampled OFDM symbol vector  $\mathbf{b}_{xL} = [b_{x[\frac{0}{L}]} \dots b_{x[\frac{NL-1}{L}}]]^T$  is given by:

$$\mathbf{b}_{xL} = \mathbf{F}^H \mathbf{d}_{x_{zp}}. \tag{1.14}$$

In (1.14) the matrix dimensions correspond to  $(NL \times NL)$ . At the increased sampling rate  $f_{os} = Lf_s$ , the length of the discrete CE is now  $N_{Lce} = N_{CE}L$  samples, while its equivalent time-domain span is still  $T_{CE} = N_{CE} \frac{T}{N}$ . Then, the oversampled version of the cyclically extended symbol in (1.10) is obtained with

---

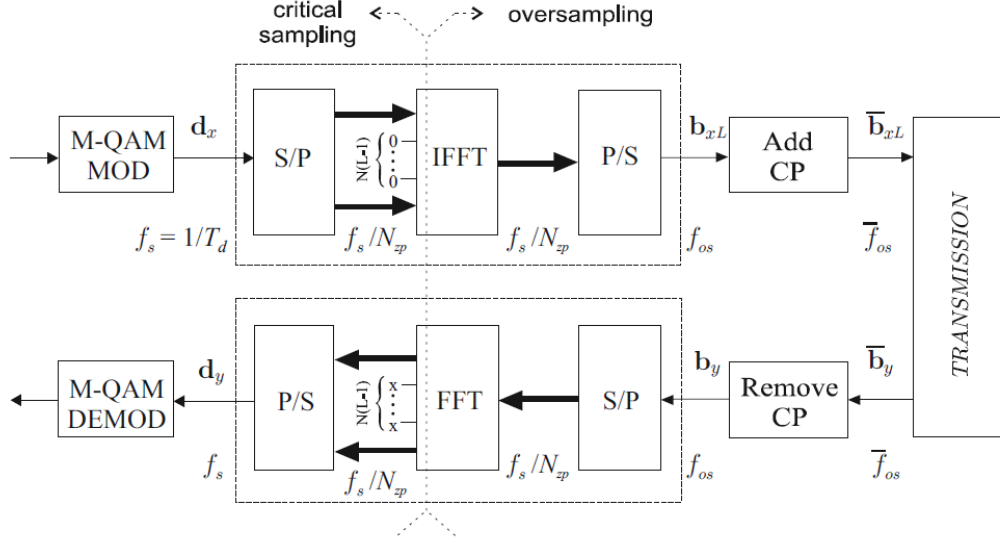


Figure 1.5: Transmission stages including oversampling [2].

$$\bar{b}_x[n/L] = \sum_{k=0}^{N-1} d_x[k] e^{j \frac{2\pi}{NL} nk} w[n/(L(N + N_{CE}) - 1)]. \quad (1.15)$$

Equivalently, using the CE operator defined in (1.12), the corresponding output vector for transmission can be expressed as

$$\bar{\mathbf{b}}_{xL} = \mathbf{P}_\eta \mathbf{F}^H \mathbf{d}_{xzp} \quad (1.16)$$

where the extension ratio is specifically  $\eta = \frac{N_{Lce}}{NL}$ . This leads to larger CE matrix dimensions but maintains the relative value of the CE over the oversampled signal length.

## 1.4 OFDM Radar Principle

Whereas in a communication system the purpose is to transmit an unknown signal in a previously estimated channel, in a radar system the transmitted signal is known, and the target and channel characteristics are usually unknown. Therefore, communications and sensing functionalities tend to be at odds with one another and are usually treated separately and with different waveforms. However, in the last years, the possibility of pursuing sensing purposes by using OFDM-based signals has been taken into consideration.

In OFDM radar applications, the evaluation of target delays is typically performed based on matched filtering implemented in the frequency domain. The signal is transformed to the frequency domain via FFT, which separates the OFDM subcarriers as shown in Figure 1.6. In frequency domain, a delay of a single reflection  $x(t)$  represents a complex exponential over the subcarrier:

$$x(t - \tau) \xrightarrow{F} X(f)e^{-j2\pi\tau f} \quad (1.17)$$

where  $X(f)$  is the spectrum of  $x(t)$ . One major difference from other radar systems is that OFDM radar operates with arbitrary OFDM waveforms generated digitally, providing adaptability and better spectral usage, and that the demodulation of the radar signal takes place in the digital domain. OFDM modulation and demodulation and distance-velocity estimation are performed based on FFTs and IFFTs, making efficient radar processing possible and enabling real-time implementation.

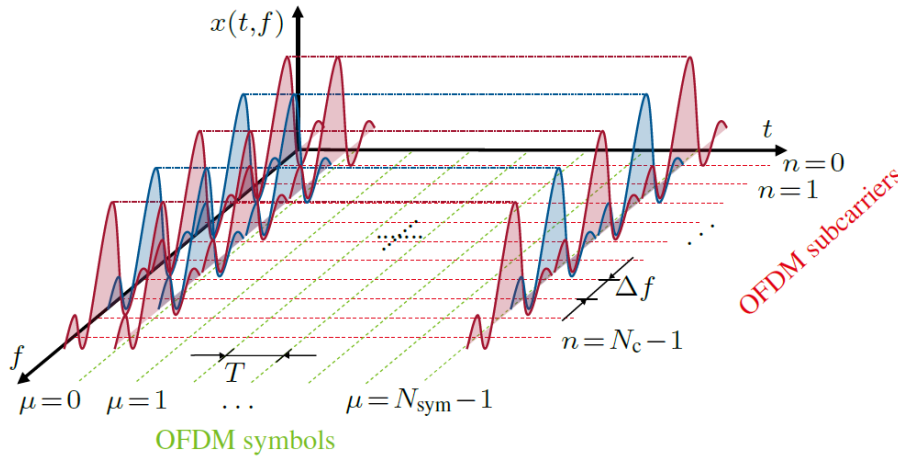


Figure 1.6: Time-frequency representation of the OFDM radar signal:  $\mu$  is the index of the OFDM symbol whereas  $N_{sym}$  is the number of OFDM symbols [5].

#### 1.4.1 High Peak-to-Average Power Ratio (PAPR)

One fundamental drawback of multicarrier signals such as OFDM, both for radar and communication, is the potentially high peak to average power ratio (PAPR). For a time domain signal  $x(t)$ , PAPR is defined as:

$$\text{PAPR} = \frac{P_{\text{peak}}}{P_{\text{avg}}} = \frac{\max(|x(t)|^2)}{\text{mean}(|x(t)|^2)} \quad (1.18)$$

---

where  $P_{\text{peak}}$  is the peak power and  $P_{\text{avg}}$  denotes the mean power. When the OFDM signal is transformed to time domain, the resulting signal is the sum of all the subcarriers, and when all the subcarriers add up in phase the result is a peak  $N$  times higher than the average power. High PAPR degrades performance of OFDM signals by forcing the analog amplifier to work in the nonlinear region, distorting the signal and making the amplifier consume more power [4]. Non-linearities in the signal chain cause distortion of the OFDM signal, leading generally to a raise of the noise floor during radar signal processing. To prevent this, the power amplifiers need to operate in the linear region, limiting the maximum power level and, as a result, a lower SNR at the receiver.

---



# Chapter 2

## 5G New Radio Physical Layer

Due to the intensive growth in demand for wireless broadband services and Internet of Things (IoT), where large numbers of smart devices communicate over the Internet, a new generation of wireless systems, 5G NR, has been developed and is now ready to be deployed. This new technology introduces several enhancements on the physical layer that enable the applicability to several fields with different requirements ( extreme broadband speed, ultralow latency, ultra-reliability, high data-rates, low error rates, ...).

5G networks and devices will require different architectures, radio access technology and physical layer algorithms. By providing higher bandwidth capacity than the current fourth generation (4G)-supporting broadband, 5G will enable a higher density of mobile broadband users and support device-to-device and massive machine-type communications. In Table 2.1 some key 5G NR parameters are compared to the previous generation 4G LTE.

	5G NR	4G LTE
E2E Latency	< 10 ms	100 ms
Connection density per km <sup>2</sup>	10 <sup>6</sup>	10 <sup>4</sup>
System spectral efficiency (bit/s)/Hz/cell	10	2.6
Peak throughput (downlink (DL)) per connection	10 Gpbs	100 Mbps

Table 2.1: Key 5G NR Parameters

### 2.1 5G Use Cases

Different application fields thought for the 5th generation of cellular networks are stated in the recommendation ITU-R M.2083 [6] and are essen-

tially three: Enhanced Mobile Broadband, Ultra-reliable and low-latency communications, and Massive machine type communications.

- *Enhanced Mobile Broadband (eMBB)* addresses the human-centric use cases for access to multi-media content, services and data providing faster connections, higher throughput and higher capacity. This usage scenario is strictly related to the constant increasing of mobile data-traffic generated by more and more data-consuming devices coupled with multimedia applications. Hence, eMBB covers a range of cases, including wide-area coverage and hotspot, finalized to a better communication experience.
- *Ultra-reliable and low-latency communications (URLLC)* has stringent requirements for capabilities such as throughput, latency and availability. This use case focuses not only on human-centric communication but there is a particular attention on machine connectivity exploiting wireless networks. Examples include vehicle-to-vehicle communication for safety, vehicle-to-infrastructure (V2I) communications, remote medical surgery and autonomous driving.
- *Massive machine type communications (mMTC)* is characterized by a very large number of connected devices. Therefore, it involves large number of transmissions of small data volumes not particularly sensitive to delays. One of the fundamental requirements for mMTC devices is to keep costs low, since it is expected a very large number of machines used in the environment, and have a long battery lifetime. This use case is typically used for consumer and industrial IoT, Industry 4.0 mission-critical machine-to-machine (MC-M2M).

## 2.2 5G Spectrum

The spectrum of 5G technology includes new frequency bands but also frequencies that were allocated for mobile networks of previous generations such as third generation (3G) and 4G LTE.

In standardization, third generation partnership project (3GPP) has focused its activities on bands where a high interest is present. The spectrum of interest can be divided into bands at low, medium, and high frequencies [7]:

- *low-frequency bands* correspond to existing LTE bands below 2 GHz, which are suitable as coverage layer, providing wide and deep coverage, including indoor. The bands with highest interest here are the 600 and
-

700 MHz bands, which correspond to 3GPP NR bands n71 and n28. Since these bands are not very wide, a maximum of 20 MHz channel bandwidth is expected in the low-frequency bands.

- *Medium-frequency bands* are in the range 3 – 6 GHz and can provide coverage, capacity, as well as high data rates through the wider channel bandwidth possible. The highest interest globally is in the range 3300 – 4200 MHz, where 3GPP has designated NR bands n77 and n78. Due to the wider bands, channel bandwidths up to 100 MHz are possible. Up to 200 MHz per operator may be assigned in this frequency range in the longer term, where carrier aggregation could then be used to deploy the full bandwidth.
- *High-frequency bands* are in the mm-Wave range above 24 GHz. They will be best suited for hotspot coverage with locally very high capacity and can provide very high data rates. The highest interest is in the range 24.25 – 29.5 GHz, with 3GPP NR bands n257 and n258 assigned. Channel bandwidths up to 400 MHz are defined for these bands, with even higher bandwidths possible through carrier aggregation.

Therefore, there is a very wide range of diverse spectrum allocations where NR can operate. The allocations vary in block size, channel bandwidth and duplex spacing supported. RF requirements for both devices and base stations are divided into two frequency ranges, as shown in Figure 2.1:

- Frequency range 1 (FR1) includes all existing and new bands below 6 GHz, where 5G NR is expected to coexist with LTE and previous generations of systems.
- Frequency range 2 (FR2) includes new bands in the range 24.25 – 52.6 GHz. This range covers a part of what is often referred to as the millimetre wave (*mm-Wave*) frequencies. At such high frequency propagation properties are different, with less diffraction, higher penetration losses and in general higher path losses. This can be compensated for by having more antenna elements both at the transmitter and receiver, to be used for narrower antenna beams with higher gain and for massive multiple-input-multiple-output (MIMO) [7].

## 2.3 Frame Structure and Numerology

In 5G NR multiple OFDM numerologies are supported, as shown in Table 2.2, where  $\mu$  and the CP for a bandwidth part are obtained from the higher-layer

---

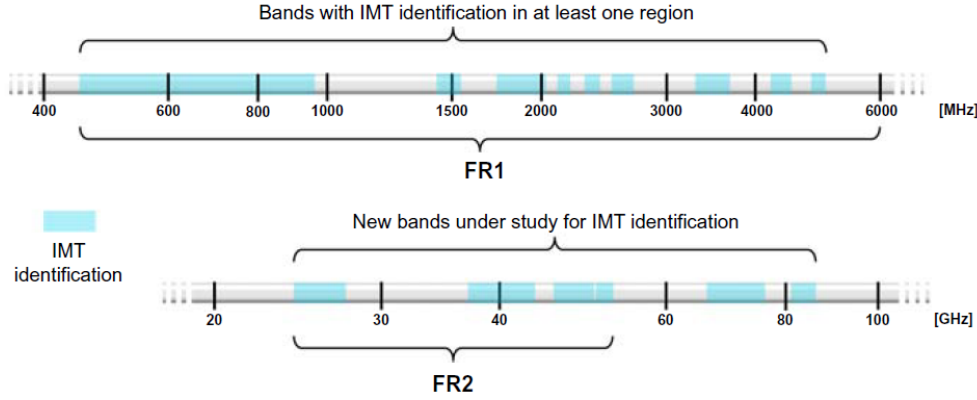


Figure 2.1: Frequency ranges FR1 and FR2 and corresponding IMT identifications. Note that the frequency scales are logarithmic [7].

parameter *subcarrier spacing* and *cyclic prefix*, respectively [8]. A bandwidth part, which will be discussed in Section 2.3.3, consists of part of the frequency band used by the device. Compared to LTE numerology, the most outstanding difference is that 5G NR supports different types of subcarrier spacing, whereas in LTE there is only one type of subcarrier spacing, equal to 15 kHz, employed in 5G NR to maintain the backward compatibility. This provides a scalable numerology that guarantees the adaptability of 5G to different scenarios with various requirements. It is commonly denoted the subcarrier spacing  $\Delta f$  depending on the parameter  $\mu$  according to  $\Delta f = 2^\mu \cdot 15$  kHz.

$\mu$	$\Delta f = 2^\mu \cdot 15[\text{kHz}]$	Cyclic prefix
0	15	Normal
1	30	Normal
2	60	Normal, Extended
3	120	Normal
4	240	Normal

Table 2.2: Possible numerologies in 5G NR

A large subcarrier spacing is beneficial from a frequency-error perspective, as it reduces the impact from frequency errors and phase noise. Another parameter strictly related to the subcarrier spacing is the CP length, as the relative overhead increases as the subcarrier spacing becomes larger, where a smaller CP would be preferable. A further version of the CP is the extended CP, which has a longer duration and is exploited when the delay spread is critical, even if it impacts on the resulting overhead. The extended cyclic

prefix can be used only when  $\Delta f = 60$  kHz, while at other spacings only normal CP is deployed.

The selection of the subcarrier spacing needs to carefully balance overhead from the CP against sensitivity to Doppler spread/shift and phase noise [7].

Numerology ( $\mu$ )	0	1	2	3	4
Subcarrier Spacing (kHz)	15	30	60	120	240
OFDM Symbol Duration ( $\mu s$ )	66.67	33.33	16.67	8.33	4.17
CP Duration ( $\mu s$ )	4.69	2.34	1.17	0.57	0.29
OFDM Symbol including CP ( $\mu s$ )	71.35	35.68	17.84	8.92	4.46

Table 2.3: OFDM Symbol Duration

### 2.3.1 Time Domain Structure

In 5G NR, physical signals are transmitted over the time domain organized as fixed size frames and subframes. A frame in NR serves as a numerology-independent time reference, as the length of each radio frame is always 10 ms. Each frame is further divided into ten equally sized subframes of 1 ms each. Frames and subframes structure is equivalent to the one adopted for LTE in order to guarantee the backward compatibility.

The radio frame structure is different depending on the type of numerology. In particular, each subframe is divided into slots consisting of 14 OFDM symbols, as shown in Figure 2.2, with a variable number of slots precisely depending on the parameter, as can be seen in Table 2.4.

$\mu$	$N_{slot}^{subframe}$	$N_{slot}^{frame(\mu)}$	$N_{slot}^{subframe(\mu)}$
0	14	10	1
1	14	20	2
2	14	40	4
3	14	80	8
4	14	160	16

Table 2.4: OFDM symbols per slot, slots per frame, slots per subframe

Since a slot is defined as a fixed number of OFDM symbols, a higher subcarrier spacing leads to a shorter slot duration. This can be used to support low-latency transmission, but as the CP shrinks when increasing the subcarrier spacing, it is not a feasible approach in all deployments. Therefore, to facilitate a reduction in the slot duration and the associated delay while

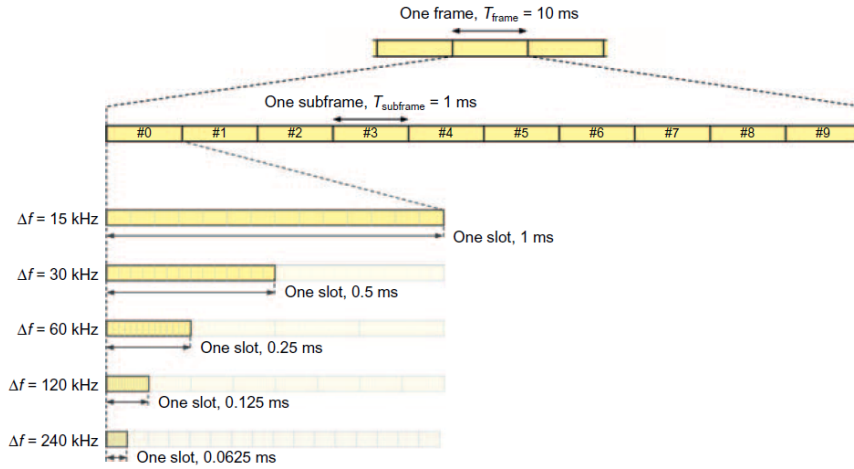


Figure 2.2: Frame, subframes and slots in NR [7].

maintaining a CP similar to the 15 kHz case, an extended CP is defined for the 60 kHz subcarrier spacing as shown in Table 2.2, at the cost of an increased overhead.

### 2.3.2 Frequency Domain Structure

The spectrum flexibility requirement points out the need for NR to be scalable in the frequency domain over a large range. Due to the scalable numerology, NR channels support bandwidth that varies from 5 to 400 MHz but devices cannot be expected to handle such wide bandwidth as it is not reasonable from a cost perspective. For this reason, they will be able to handle only a part of the frequency band, specified as a maximum number of physical resource blocks (PRBs). Furthermore, the part of the frequency band received by a specific user equipment may not be centred around the carrier frequency and each NR device may have its direct current (DC) located at different locations in the available frequency band (unlike LTE where all devices have the DC coinciding with the carrier frequency). This enforces the deployment of DC subcarriers, as illustrated in Figure 2.3, which do not carry useful data but instead are used by each device to discover the centre of the bands where transmission takes place.

The elementary unit defined in the frequency domain is referred to as resource element (RE), consisting of one OFDM symbol upon one subcarrier and it is denoted by a pair  $(k, i)_{p, \mu}$ , where  $k$  is the frequency index and  $i$  represents the symbol time index,  $p$  is the antenna port, and  $\mu$  is the scaling factor. Furthermore, as illustrated in Figure 2.4, a set of 12 consecutive

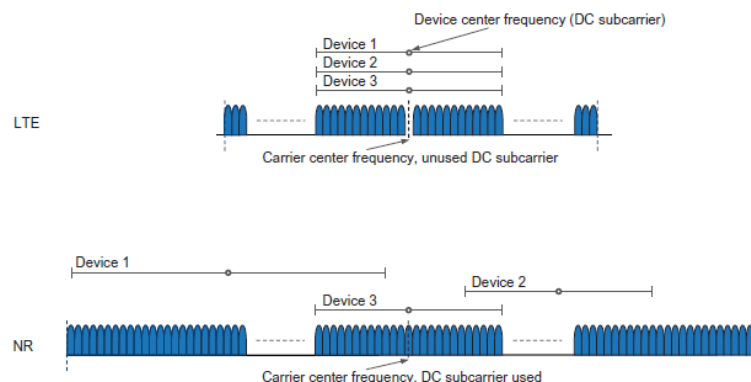


Figure 2.3: Handling of the DC subcarrier in LTE and NR [7].

subcarriers along one OFDM symbol (that is 12 RE) is called resource block (RB). Unlike LTE, where transmission occupies a complete slot, in NR the RB is defined just in the frequency domain due to the flexibility in time duration for different transmission.

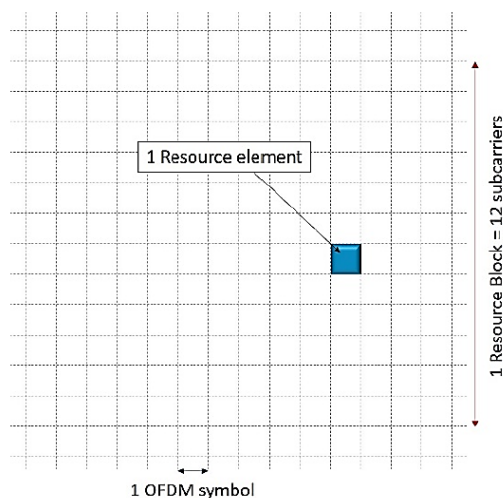


Figure 2.4: Resource grid and resource element in 5G [7].

The alignment in the frequency domain is maintained as one RB having a subcarrier spacing of  $2\Delta f$  covers the interval of frequencies occupied by two RBs at with subcarrier spacing  $\Delta f$ . The alignment among RBs at different scaling factors is maintained through the definition of resource grids, where there is one resource grid per subcarrier spacing and antenna port. A resource grid consists of  $N_{grid,y}^{size,\mu} \times N_{SC}^{RB}$  subcarriers in the frequency domain and  $N_{symp}^{subframe,\mu}$  OFDM symbols in the time domain, where  $N_{grid,y}^{size,\mu}$  is the specific

carrier bandwidth adopted for scaling factor  $\mu$  on the channel with direction  $y$  that may be either DL or uplink (UL) while  $N_{SC}^{RB}$  is the number of subcarriers per RB [8].

As 5G NR supports multiple numerologies and not all devices may support the full carrier bandwidth, in order to indicate the RB within the carrier where the transmission takes place it is used a common reference point called *point A*, together with two types of RBs: common resource block (CRB) and PRB. There is a third type of RB, *virtual resource block*, which are mapped to PRB when describing the mapping of the physical shared channels PDSCH/PUSCH.

- *Point A* is the subcarrier 0 of CRB 0 for every scaling factor, and it is used to map PRB to the corresponding CRB. Point A may be located outside the actual carrier.
- *Common Resource Blocks*, given  $\mu$ , are numbered from 0 and upwards in the frequency domain and the center of their subcarrier 0 is the reference point A. If  $n_{CRB}^\mu$  is the index of CRB, then it holds that  $n_{CRB}^\mu = \lfloor \frac{k}{N_{SC}^{RB}} \rfloor$  where  $k$  is the subcarrier index relatively to point A.
- *Physical resource blocks* (PRB), which are used to describe the actual transmitted signal, are labeled through a number between 0 and  $N_{BWP,b}^{size}$ , where  $b$  is the number of bandwidth part, which will be discussed in the next section. The mapping between CRBs and PRBs is  $n_{CRB} = n_{PRB} + N_{BWP,b}^{start}$  with  $n_{CRB}$  being the number of CRB,  $n_{PRB}$  the number of PRB, and  $N_{BWP,b}^{start}$  the initial CRB of the bandwidth part with respect to the CRB 0.

### 2.3.3 Bandwidth Part

Given the very wide carrier bandwidth supported in 5G NR, if the same approach as in LTE is used, where the DL control channels can occupy the full carrier bandwidth, it would result in an increase of power consumption of the device. Therefore, in NR, devices can use narrower bandwidth for receiving small-to-medium sized data transmissions and open the full bandwidth only when a large amount of data is scheduled, allowing a *receiver-bandwidth adaptation*. Hence, a bandwidth part (BWP) is defined as a set of contiguous PRBs for a fixed numerology and is described through two parameters:  $N_{BWP,b}^{start,\mu}$  as the starting RB of the  $b$ th bandwidth part and  $N_{BWP,b}^{size,\mu}$  being the size of the bandwidth part itself. Therefore, bandwidth parts identify the PRBs where each user is able to handle the communication. Furthermore,

---

each user is designed in such a way to receive only one numerology per time. Each device can be assigned up to four bandwidth parts for DL and up to four additional bandwidth parts for the UL. When a user has to initiate a connection, it receives from the physical broadcast channel (PBCH) the initial bandwidth part for the DL, while the physical downlink control channel (PDCCH) signals the initial bandwidth part for the UL [8]. In Figure 2.5 it is illustrated an example of how the device switches to a bigger BWP when a large amount of data is transmitted.

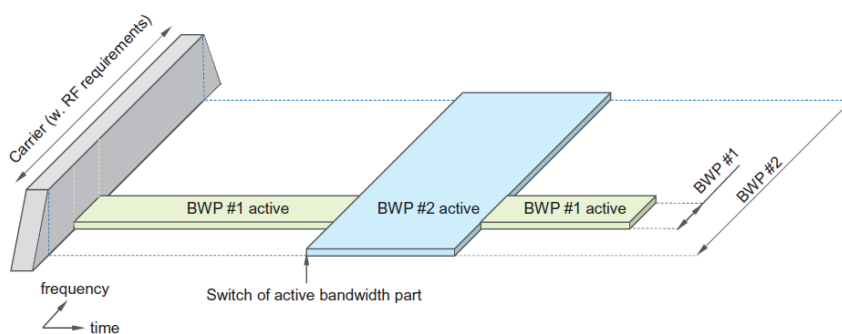


Figure 2.5: Example of bandwidth adaptation using bandwidth parts [7].

### 2.3.4 Transmission Techniques

NR has been designed in order to support both time division duplex (TDD) and frequency division duplex (FDD) schemes.

In *Time Division Duplex* transmissions, UL and DL are allocated on the same subcarrier but on different time slots in order to guarantee the nonoverlapping in time domain. In TDD scheme it is necessary to reserve a guard period where neither UL nor DL transmissions occur and to guarantee a transient period to switch from a direction to the other. The length of the guard period is proportional to the cell size, hence it increases as the distance from the base station gets higher. This type of scheme is particularly useful in small-cell deployments.

In *Frequency Division Duplex* UL and DL transmissions happen simultaneously in the time domain while they are assigned to different subcarriers in the frequency domain, denoted  $f_{UL}$  and  $f_{DL}$ , hence UL and DL channels are distinguished within the entire available bandwidth. This scheme requires filtering operations both in transmission and reception, known as duplex filtering, in order to guarantee the UL and DL separation in the frequency domain.



# Chapter 3

## OFDM Radar

### 3.1 OFDM Radar Estimation Problem

In order to develop algorithms able to perform radar sensing based on 5G NR systems and their downlink transmit signal, as anticipated in Section 1.4, it is essential to understand how OFDM signals behave when used mainly for radar purposes. This is necessary since 5G signals are based on a OFDM signal type.

Generally, in a basic monostatic radar system, both transmitter and receiver are implemented on the same device. To obtain the radar image, a signal  $b_x(t)$  is transmitted. Subsequently, the radar receives a signal  $b_y(t)$ , which consists of a superposition of signals reflected both from the desired target and from other objects positioned nearby, to which the receiver noise is added, as shown in Figure 3.1. The radar system then analyzes the received signal to determine range and relative velocity of the targets. For this chapter, only one antenna at the transmitter is assumed, which operates as the receiver as well, and that the radar is not attempting to estimate the direction of arrival of the backscattered signal.

Assuming a total of  $H$  reflecting objects, the received signal has the form [9]:

$$b_y(t) = \sum_{h=0}^{H-1} a_h b_x(t - \tau_h) e^{j2\pi f_{D,h} t} e^{j\tilde{\varphi}_h} + \tilde{z}(t) \quad (3.1)$$

where the magnitude of every signal reflection is attenuated by a factor  $a_h$ . This factor depends on the distance of the target  $r_h$  and its radar cross

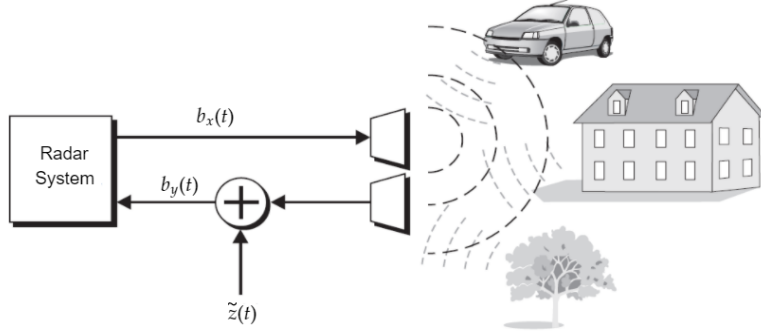


Figure 3.1: Schematic of a radar system [9].

section (RCS),  $\sigma_{\text{RCS},h}$ . The attenuation can be written as:

$$a_h = \sqrt{\frac{Gc_0^2\sigma_{\text{RCS},h}}{(4\pi)^3r_h^4f_c^2}} \quad (3.2)$$

where  $G$  is the antenna gain,  $c_0$  is the speed of light and  $f_c$  is the carrier frequency of the radio frequency (RF) signal. The signal is delayed by a quantity  $\tau_h$ , which is the time it takes for it to travel from the transmitter to the target and receive back at the origin:

$$\tau_h = 2\frac{r_h}{c_0}. \quad (3.3)$$

A moving target with relative velocity  $v_{\text{rel},h}$  will cause a Doppler shift in the frequency expressed as:

$$f_{\text{D},h} = 2\frac{v_{\text{rel},h}}{c_0}f_c. \quad (3.4)$$

Furthermore, the signal is rotated by an additional random phase  $\tilde{\varphi}_h$ . Finally, AWGN,  $\tilde{z}(t)$ , is added to the receiving signal.

A new notation is introduced to apply the (3.1) to OFDM signals. A transmitted OFDM frame is represented by a matrix

$$\mathbf{G}_{\text{Tx}} = \begin{pmatrix} d_x(0,0) & \cdots & d_x(0,M-1) \\ d_x(1,0) & \cdots & d_x(1,M-1) \\ \vdots & \ddots & \vdots \\ d_x(N-1,0) & \cdots & d_x(N-1,M-1) \end{pmatrix} \in \mathbf{A}^{N \times M} \quad (3.5)$$

where each row of  $\mathbf{G}_{\text{Tx}}$  represents a subcarrier, each column represents a different OFDM symbol of the transmitted frame and  $A \in \mathbb{C}$  is the complex

modulation alphabet. The frequency of the  $k$ -th subcarrier is denoted by  $f_k = f_0 + k\Delta f$ . If some subcarriers are left empty (such as the DC carrier), the corresponding elements  $d_x(k, i)$  are set to zero. Usually, empty subcarriers at the edge, used as guard bands, are not present in the transmitted matrix, therefore  $\mathbf{G}_{\text{Tx}}$  has  $N < N_{\text{IFFT}}$  rows, where  $N$  is the number of active subcarriers and  $N_{\text{IFFT}}$  is the dimension of the IFFT at the modulator.

Symbol	Parameter
$A$	Modulation alphabet
$N$	Number of active subcarriers
$M$	Number of OFDM symbols
$\Delta f$	subcarrier spacing
$T = \frac{1}{\Delta f}$	OFDM symbol duration
$T_{\text{CE}}$	Cyclic Prefix duration
$T_1 = T + T_{\text{CE}}$	Total duration of one OFDM symbol
$N_{\text{IFFT}} \geq N$	IFFT length
$f_s = N_{\text{IFFT}}\Delta f$	Sampling rate

Table 3.1: Parameters in an OFDM transmitter

By modulating the  $\mathbf{G}_{\text{Tx}}$  matrix, in combination with the knowledge of the parameters given in Table 3.1, the time domain signal can be obtained and, vice versa, the matrix can easily be obtained by demodulating the time domain signal.

In particular, at the receiver the signal backscattered from the target is demodulated to obtain the received frame matrix  $\mathbf{G}_{\text{Rx}}$ , by performing analog to digital conversion, removal of the CP, and lastly the calculation of an FFT of length  $N_{\text{IFFT}}$  for every column of the matrix.

Theoretically, the received matrix  $\mathbf{G}_{\text{Rx}}$  can be obtained given a transmit matrix and a set of  $H$  reflecting targets. To simplify this, it is assumed at first that only one object is present ( $H = 1$ ) in order to easily analyze the effects of each target.

A frequency shift by  $f_{\text{D}}$  is simply a modulation of every row of  $\mathbf{G}_{\text{Tx}}$  with a discretely sampled complex sinusoid  $e^{j2\pi f_{\text{D}} T_1 i}$ ,  $i = 0, \dots, M - 1$ .

Differently, the time delay causes a phase shift of the individual elements  $d_x(k, i)$  and the phase shift value is different for every subcarrier, depending on its frequency. For a delay  $\tau$ , the phase shift on the  $k$ -th subcarrier is thus  $e^{-j2\pi(k\Delta f + f_0)\tau}$ . By combining these effects,  $\mathbf{G}_{\text{Rx}}$  for  $H = 1$  becomes [9]:

$$(\mathbf{G}_{\text{Rx}})_{k,i} = a_0 (\mathbf{G}_{\text{Tx}})_{k,i} e^{j2\pi T_1 f_{\text{D},0} i} e^{-j2\pi \tau_0 (k\Delta f + f_0)} e^{j\tilde{\varphi}_0} + (\tilde{\mathbf{Z}})_{k,i} \quad (3.6)$$

where  $\tilde{\mathbf{Z}} \in \mathbb{C}^{N \times M}$  is the matrix representation of the AWGN at the receiver. Its elements are i.i.d. complex random variables from a circular, zero-mean Gaussian distribution with variance  $\sigma^2$ . As  $f_0$  and  $\tilde{\varphi}_0$  are constant, another notation can be defined  $\varphi_0 := \tilde{\varphi}_0 - 2\pi f_0 \tau_0$  and thus (3.6) can be simplified to:

$$(\mathbf{G}_{\text{Rx}})_{k,i} = a_0 (\mathbf{G}_{\text{Tx}})_{k,i} e^{j2\pi T_1 f_{\text{D},0} i} e^{-j2\pi k \tau_0 \Delta f} e^{j\varphi_0} + (\tilde{\mathbf{Z}})_{k,i}. \quad (3.7)$$

As  $\mathbf{G}_{\text{Tx}}$  serves no purpose for the estimation problem, it is removed from the equation by element-wise division:

$$(\mathbf{G})_{k,i} = \frac{(\mathbf{G}_{\text{Rx}})_{k,i}}{(\mathbf{G}_{\text{Tx}})_{k,i}} = a_0 e^{j2\pi T_1 f_{\text{D},0} i} e^{-j2\pi k \tau_0 \Delta f} e^{j\varphi_0} + \frac{(\tilde{\mathbf{Z}})_{k,i}}{(\mathbf{G}_{\text{Tx}})_{k,i}}. \quad (3.8)$$

Another notation is introduced in order to remove the influence of the transmitted data from the model. In particular, an alternative noise matrix  $(\mathbf{Z})_{k,i} = (\tilde{\mathbf{Z}})_{k,i} / (\mathbf{G}_{\text{Tx}})_{k,i}$  can be defined since the elements of  $\tilde{\mathbf{Z}}$  are from a circular, zero-mean Gaussian distribution and a division by a phase matrix preserves its statistics. Therefore  $\mathbf{Z}$  is still a white noise process if  $\tilde{\mathbf{Z}}$  is white. Having defined  $\mathbf{Z}$ ,  $\mathbf{G}$  can be written as

$$(\mathbf{G})_{k,i} = a_0 e^{j2\pi T_1 f_{\text{D},0} i} e^{-j2\pi k \tau_0 \Delta f} e^{j\varphi_0} + (\mathbf{Z})_{k,i}. \quad (3.9)$$

Since all operations used to calculate  $\mathbf{G}_{\text{Rx}}$  from  $b_y(t)$  (FFT and removal of the CP) are linear with respect to their input signal, the sum from (3.1) can be reintroduced and the following expression can be obtained:

$$(\mathbf{G})_{k,i} = \sum_{h=0}^{H-1} a_h e^{j2\pi T_1 f_{\text{D},h} i} e^{-j2\pi k \tau_h \Delta f} e^{j\varphi_h} + (\mathbf{Z})_{k,i}. \quad (3.10)$$

One advantage comes from the fact that calculations of Doppler and delay are entirely separate. As is the case for FMCW radar systems, they do not impact each other and can be estimated independently.

From (3.10), a generic target estimation problem can be articulated as follows:

1. Estimation of the number of targets.
  2. For every target, estimation of the respective frequencies  $\hat{\Omega}_r$  (column-wise) and  $\hat{\Omega}_v$  (row-wise) of the sinusoids.
-

3. Translation of these frequencies into distance and relative velocity using the following expressions, which represent the basic distance and velocity resolutions in the range-Doppler map:

$$\hat{r} = \frac{1}{2}\hat{\tau}c_0 = \frac{\hat{\Omega}_d c_0}{2(2\pi)\Delta f}, \quad (3.11)$$

$$\hat{v} = \frac{\hat{f}_D c_0}{2f_c} = \frac{\hat{\Omega}_v c_0}{2(2\pi)f_c T_1}. \quad (3.12)$$

### 3.1.1 Interpolation

The 5G NR technology (as well as the LTE one) transmit grids contain unused subcarriers within the transmit signal, whose location vary from OFDM symbol to another. The direct calculation of (3.10) is therefore not feasible in these point, but is carried out only for the active subcarriers. Therefore, before target detection and range-velocity estimation, the radar processing proposed in [13] adopts linear interpolation across OFDM symbols and, thus, defines the interpolated grid sample  $(\bar{\mathbf{G}})_{k,l}$  at an unused subcarrier  $k$  of an OFDM symbol  $i$  as:

$$(\bar{\mathbf{G}})_{k,i} = (\mathbf{G})_{k,i} + \left( \frac{\mathbf{G}_{k,i_2} - \mathbf{G}_{k,i_1}}{i_2 - i_1} \right) (i - i_1) \quad (3.13)$$

where  $i_1 < i < i_2$  and the subcarrier  $k$  is assumed to be active at OFDM symbols  $i_1$  and  $i_2$ . In case of unused subcarriers in the first or last symbol of the transmitted grid, (3.13) cannot be used, therefore the calculation of (3.10) is still not feasible. In this work these symbols are simply calculated using (3.13), considering  $i_1$  and  $i_2$  such that  $i < i_1 < i_2$  for the unused subcarrier  $k$  in the first OFDM symbol, and  $i_1 < i_2 < i$  for the unused subcarrier  $k$  in the last OFDM symbol.

## 3.2 Periodogram-based Estimation Algorithms

The actual radar processing building on the known transmit waveform can be implemented in multiple ways, either with time domain or subcarrier-domain processing [13]. In this work, the subcarrier-domain processing, utilizing directly the transmit and receive grids of samples,  $\bar{\mathbf{G}}_{\text{Tx}}$  and  $\bar{\mathbf{G}}_{\text{Rx}}$  respectively, is adopted.

---

The input data for the periodogram is the matrix  $\bar{\mathbf{G}}$ , obtained through element-wise division between the transmit and receive matrix, as shown in (3.10), and interpolation. Then the periodogram is calculated as follows:

$$\mathbf{Per}_{\bar{\mathbf{G}}}(n, m) = \underbrace{\left| \sum_{k=0}^{N_{\text{Per}}-1} \left( \sum_{i=0}^{M_{\text{Per}}-1} (\bar{\mathbf{G}})_{k,i} e^{-j2\pi \frac{im}{M_{\text{Per}}}} \right) e^{j2\pi \frac{kn}{N_{\text{Per}}}} \right|^2}_{\text{IFFT of length } N_{\text{Per}}}. \quad (3.14)$$

FFT of length  $M_{\text{Per}}$

Choosing a value of  $M_{\text{Per}} > M$  and  $N_{\text{Per}} > N$ , hence increasing the number of points of the discrete periodogram, will increase the accuracy of the estimation at high SNR values [12]. For this work  $M_{\text{Per}}$  and  $N_{\text{Per}}$  are set to  $M$  and  $N$  respectively.

The resulting matrix directly represents a two-dimensional radar image in range and Doppler. The sinusoids in  $\bar{\mathbf{G}}$  will result in a peak in  $\mathbf{Per}_{\bar{\mathbf{G}}}(n, m)$ , which will be detected in order to estimate the position and velocity of the target. Then, if  $\mathbf{Per}_{\bar{\mathbf{G}}}(\hat{n}, \hat{m})$  corresponds to a peak value,  $\bar{\mathbf{G}}$  will present a column-wise oscillation of frequency  $\hat{\Omega}_r = 2\pi\hat{n}/N_{\text{Per}}$  caused by the propagation delay, and a row-wise oscillation of frequency  $\hat{\Omega}_v = 2\pi\hat{m}/M_{\text{Per}}$  caused by the Doppler shift. Now, by applying  $\hat{n}$  and  $\hat{m}$ , respectively to (3.11) and (3.12), it is possible to rewrite them as:

$$\hat{r} = \frac{\hat{n}c_0}{2\Delta f N_{\text{Per}}}, \quad (3.15)$$

$$\hat{v} = \frac{\hat{m}c_0}{2f_c T_1 M_{\text{Per}}}. \quad (3.16)$$

Therefore, once the values  $\hat{n}$  and  $\hat{m}$  which maximize the periodogram are found, it is simply necessary to insert them into (3.15) and (3.16), respectively, in order to obtain the distance and velocity estimations. The indices  $n$  and  $m$  are chosen such that

$$n = 0, \dots, N_{\text{Per}} - 1 \quad \text{and} \quad m = \left\lfloor \frac{-M_{\text{Per}}}{2} \right\rfloor, \dots, \left\lfloor \frac{M_{\text{Per}}}{2} \right\rfloor - 1. \quad (3.17)$$

Since Doppler shifts can be negative (and correspond to targets moving away from the sensor),  $m$  is shifted symmetrically around the zero, whereas negative distances have no physical meaning. Any periodogram-based estimate must therefore automatically lie within the intervals  $0 \leq \hat{r} \leq r_{\text{max}}$  and  $-v_{\text{rel,max}} \leq \hat{v} \leq v_{\text{rel,max}}$  in order to find the discrete values which are closest

to the real values  $\tau_0$  and  $f_{D,0}$ .

The resolution for the distance estimation, determined by the observation time of the transmitted pulse in conventional radar systems, is determined by the bandwidth over which the delay-induced complex exponentials are observed. Thus, the inverse of the bandwidth BW determines the resolution with which the delays  $\Delta\tau = 2\Delta r/c_0$  are measured, which leads to

$$\Delta r = \frac{c_0}{2\text{BW}} = \frac{c_0}{2\Delta f N} \quad (3.18)$$

for the distance resolution. For the last identity in (3.18),  $\text{BW} = N\Delta f$  is used.

Analogously, the velocity resolution is determined by the observation time of the Doppler-induced complex exponentials. The Doppler resolution  $\Delta f_D = 2\Delta v f_c/c_0$  leads to the following expression for the velocity resolution:

$$\Delta v = \frac{c_0}{2f_c T_1 M}. \quad (3.19)$$

Figure 3.2 shows a block diagram of an entire OFDM radar system.

Given that the CP duration,  $T_{\text{CE}}$ , is assumed larger than the propagation time of the reflected signal to the furthest target and back, and  $\Delta f$  is at least one order of magnitude larger than the largest Doppler shift, as will be later discussed in Section 3.2.3, then the indices  $n$  and  $m$  can be chosen in order to analyze the periodogram only in determined *search ranges* [12]. If CP is a fraction of the OFDM symbol used as cyclic prefix (typically  $\text{CP}=1/4$ ), and D is a fraction of subcarrier distance the Doppler shift can maximally be (typically  $\text{D}=1/10$ ), then maximum values for  $n$  and  $m$  are defined as:

$$\begin{aligned} n_{\max} &= [\text{CP} \cdot N_{\text{Per}}], \\ m_{\max} &= [\text{D} \cdot M_{\text{Per}}]. \end{aligned} \quad (3.20)$$

Having defined these maximum values, the periodogram of (3.14) can be computed in the range  $-m_{\max}, \dots, m_{\max}$  for the velocities and  $0, \dots, n_{\max}$  for the distances.

### 3.2.1 Distance Estimation Parameters

In radar applications, the *range resolution* is defined as the minimum distance between two targets for which it is possible to distinguish both targets without ambiguity and can be estimated through (3.18), given in Section 3.2. The distance estimation for OFDM radar is based on the processing of delay-induced complex exponentials. Hence, the subcarrier spacing  $\Delta f$  corresponds

---

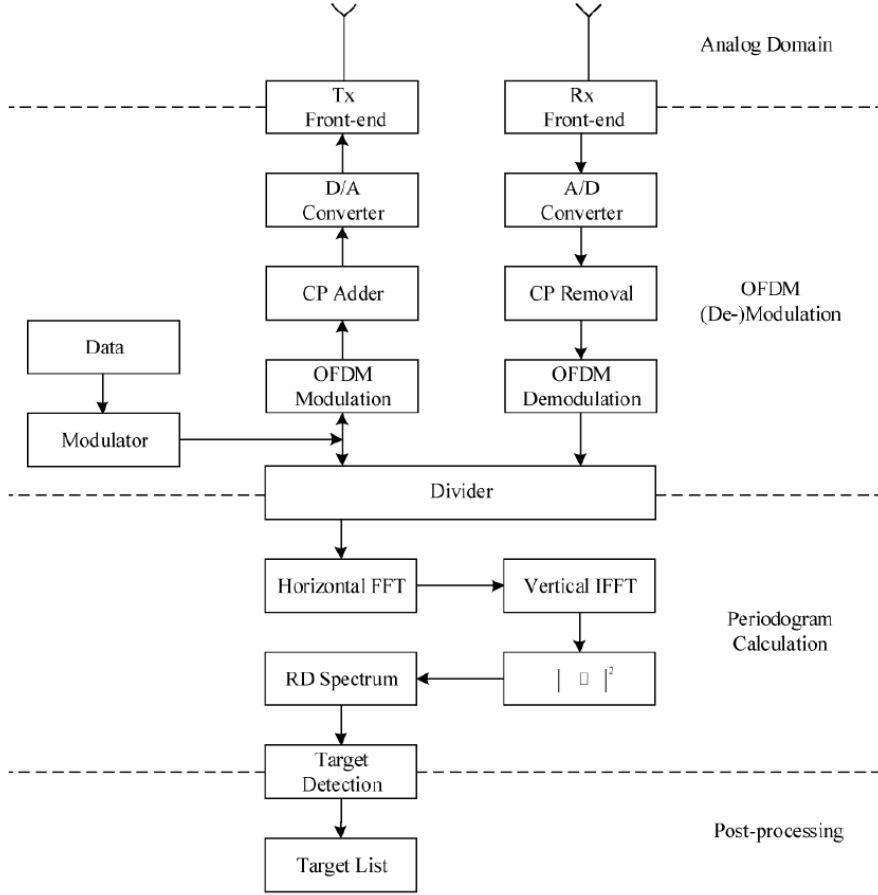


Figure 3.2: Block diagram of a periodogram-based OFDM radar system [10].

to the sampling step with which these complex exponentials are sampled, and thus determines the maximum *unambiguously measurable range* of delays. Therefore, the maximum unambiguously measurable delay  $\tau_h = 2r_h/c_0$  is determined by considering  $|\tau\Delta f| < 1$ , given the discrete nature of  $\bar{\mathbf{G}}$ , which leads to

$$r_{\text{unamb}} = \frac{\tau_{\text{unamb}}c_0}{2} = \frac{c_0}{2\Delta f}. \quad (3.21)$$

Another distance parameter of interest is the maximum distance detectable  $r_{\text{max}}$ . This parameter is determined by the duration of the CP and typically needs to be set to the maximum distance from which potentially considerable reflection power can be expected. Thus, based on the chosen  $T_{\text{CE}}$  duration, the maximum distance can be written as:

$$r_{\max} = \frac{T_{\text{CE}}c_0}{2}. \quad (3.22)$$

### 3.2.2 Velocity Estimation Parameters

The *velocity resolution* is defined as the minimum difference of radial velocity between two targets at the same distance from the radar for which it is possible to distinguish both targets without ambiguity and can be estimated through (3.19), given in Section 3.2.

The velocity estimation for OFDM radar is performed through estimation of Doppler-induced complex exponentials over the consecutive OFDM symbols, therefore, they represent the sampling points. Hence, the maximum unambiguously measurable Doppler frequency is  $f_{\text{D},h} = 2v_{\text{rel},h}f_c/c_0$  and the unambiguously measurable velocity range is determined, considering  $|T_1 f_{\text{D}}| < 1/2$ , as:

$$v_{\text{unamb}} = \frac{c_0}{2f_c T_1}. \quad (3.23)$$

The velocity estimation typically exhibits both positive and negative frequencies. Therefore, the unambiguous velocity range  $v_{\text{unamb}}$  needs to be set such that both positive and negative velocities are detected unambiguously. As (3.19) and (3.23) show, the velocity estimation parameters depend on the carrier frequency. The higher the carrier frequency, the less the unambiguous velocity range and the better the velocity resolution.

### 3.2.3 OFDM Radar Parametrization

The validity of the signal model given in (3.10) implies the following assumptions, that guarantee that the OFDM symbols received can be correctly demodulated and simplify the design of the algorithm:

1.  $T_{\text{CE}}$  is larger than the propagation time required for the signal to travel to the furthest target and go back to the receiver.
  2. The Doppler shift of OFDM subcarriers is assumed insignificant for all targets. This requires the subcarrier spacing  $\Delta f$  to be much larger than the maximum expected (positive or negative) Doppler shift  $f_{\text{D},\max}$ , i.e.  $\Delta f \geq 10|f_{\text{D},\max}|$ .
  3. All the subcarriers are affected by the same Doppler shift. The carrier frequency  $f_c$  is larger than the signal's bandwidth, i.e.,  $\text{BW} \ll f_c$ . This can be interpreted as *narrowband assumption*, i.e. assumption that all frequencies in the signal are influenced identically by the channel.
-

4. During one OFDM radio frame the target's position can be assumed constant if the measurement is lower than the distance resolution of the radar when the relative velocity is small enough.
5. The modulation system is normalized to unit power. This assumption is always verified for constant-modulus alphabets such as phase shift keying (PSK) [12].

### 3.2.4 Signal-to-Noise Ratio and Processing Gain

Generally, the SNR is defined as the power of the received signal divided by the power of the noise present in the signal bandwidth. Due to the normalization to unit signal power, SNR can be simply defined by the noise power [12]:

$$\text{SNR} = -10 \log_{10} \sigma^2. \quad (3.24)$$

In the next chapter this will be taken into better consideration in order to determine the noise variance  $\sigma^2$  for different scenarios.

When a target is present, the backscattered signal power  $P_{\text{Rx}}$  can be expressed as:

$$P_{\text{Rx}} = \frac{P_{\text{Tx}} G c_0^2 \sigma_{\text{RCS}}}{(4\pi)^3 f_c^2 r^4} \quad (3.25)$$

where  $P_{\text{Tx}}$  is the transmit power and  $G$  is the antenna gain. The relevant SNR, calculated before the signal processing in the matrix  $\tilde{\mathbf{G}}_{\text{Rx}}$ , is given by:

$$\text{SNR}_{\tilde{\mathbf{G}}_{\text{Rx}}} = \frac{P_{\text{Rx}}}{k_{\text{B}} \theta \cdot \text{NF} \cdot N \Delta f} \quad (3.26)$$

where the noise power density, expressed as  $k_{\text{B}} \theta \cdot \text{NF}$ , consists of the Boltzmann constant  $k_{\text{B}}$ , the temperature  $\theta$  and the noise figure NF, which incorporates the noise from all the components of the receiver chain, including the ADC. By multiplying this by the actual occupied bandwidth ( $N \Delta f$ ), this becomes the total noise power.

The division by  $\tilde{\mathbf{G}}_{\text{Tx}}$  in (3.10) does not change the SNR, as it affects noise and received power alike. The matrix  $\tilde{\mathbf{G}}$  thus has the same SNR as the matrix  $\tilde{\mathbf{G}}_{\text{Rx}}$ ,

$$\text{SNR}_{\tilde{\mathbf{G}}} = \text{SNR}_{\tilde{\mathbf{G}}_{\text{Rx}}}. \quad (3.27)$$

However, the target detection is performed on the periodogram, not on  $\tilde{\mathbf{G}}$ . Its signal-to-noise ratio,  $\text{SNR}_{\text{Per}}$ , is therefore defined for the bin containing

the target's corresponding peak only. In each Fourier transform the signals add in a coherent deterministic process, resulting in a total power gain of  $N^2$  from the outer sum in (3.14) and of  $M^2$  from the inner sum, therefore a total power gain of  $(NM)^2$ , whereas noise, as a stochastic quantity, only experiences a power gain of  $NM$  [11]. This results in a processing gain  $PG$  in the logarithmic scale equal to

$$PG = 10 \log_{10}(NM). \quad (3.28)$$

This results in

$$\text{SNR}_{\text{Per}} = \text{SNR}_{\mathbf{G}} + PG. \quad (3.29)$$

More energy is backscattered towards the receiver when multiple targets are present, but if the targets are far apart this has little effect on the SNR in one individual bin of the periodogram.

### 3.2.5 Window Functions

Window functions are usually applied to the input data in periodogram-based spectral estimation. Usually, for any signal processing the main motivation for windowing is to reduce sidelobes in the discrete time Fourier Transform (DTFT). Windows reduce the energy in the data and its effective time domain duration by tapering the data near the edges. The reduction in energy is reflected in the DTFT as a reduction in the peak value. By reciprocal spreading property, the reduced effective width of the data in the time domain is reflected in a wider main lobe of its DTFT in the frequency domain. Thus, the frequency resolution of the DTFT is degraded [14].

Window functions have two main features: the width of the main lobe  $\Omega_s$ , where  $-\pi \leq \Omega_s \leq \pi$ , and the sidelobe attenuation  $a_{min}$ , expressed in dB. The costs of windowing are offset by a great reduction in sidelobes levels, depending on the window shape, which is useful for reliable detection of targets.

In this case a two-dimensional window matrix  $\mathbf{W} \in \mathbb{R}^{N \times M}$  is defined, which is multiplied element-wise with the matrix  $\bar{\mathbf{G}}$ . The expression in (3.14) is thus refined to

$$\text{Per}_{\mathbf{G}}(n, m) = \underbrace{\left| \sum_{k=0}^{N_{\text{Per}}-1} \left( \overbrace{\sum_{i=0}^{M_{\text{Per}}-1} (\bar{\mathbf{G}})_{k,i} (\mathbf{W})_{k,i} e^{-j2\pi \frac{im}{M_{\text{Per}}}}}_{\text{FFT of length } M_{\text{Per}}} \right) e^{j2\pi \frac{kn}{N_{\text{Per}}}} \right|^2}_{\text{IFFT of length } N_{\text{Per}}}. \quad (3.30)$$

The window matrices are designed by calculating the outer product of two one-dimensional windows,

$$\mathbf{W} = \frac{1}{\|\mathbf{w}_d\|^2 \|\mathbf{w}_v\|^2} \mathbf{w}_d^T \otimes \mathbf{w}_v \quad (3.31)$$

with  $\mathbf{w}_d \in \mathbb{R}^{1 \times N}$  and  $\mathbf{w}_v \in \mathbb{R}^{1 \times M}$ . The normalization factor is introduced to ensure that the total energy in the periodogram is independent of the chosen window matrix. An extensive study on various windows is present in [15]. The following window types are of interest for the OFDM radar applications:

1. *Rectangular window*: this actually represents no windowing at all (other than enforcing a finite length to the data) and can be interpreted as a “lack” of a window function, having a constant value for all samples:

$$(\mathbf{w}_d)_k = 1 \quad k = 0, \dots, N - 1. \quad (3.32)$$

The rectangular window has the smallest main lobe width (which is optimal for the radar resolution). However, it also has the smallest side lobe attenuation (which is bad for the dynamic range), which makes it generally not a good choice for the radar system.

2. *Hamming window*: compared to the rectangular window, this window has a higher sidelobe attenuation, but twice the main lobe width.
3. *Dolph-Chebyshev window*: this window is defined in the frequency domain in terms of uniformly spaced samples of the window’s Fourier transform. Furthermore, the sidelobe level can be configured according to the required dynamic range and determines the main lobe width.

### SNR Loss by Windowing

Windowing does not change the SNR at the input of the periodogram, since noise and signal are influenced in the same way by element-wise multiplication with  $W$ . However, since the main lobe’s widths differ between according to the window of preference, the height of their peaks also varies, resulting in an SNR loss that needs to be taken into account into the processing gain. The processing gain is therefore calculated as:

$$\text{PG} = 10 \log_{10}(NM) + \text{SNR}_{\mathbf{w}_d} + \text{SNR}_{\mathbf{w}_v} \quad (3.33)$$

where  $\text{SNR}_{\mathbf{w}_d}$  and  $\text{SNR}_{\mathbf{w}_v}$  are the SNR losses for the row and column-wise windows, respectively. They are given by

---

$$\text{SNR}_{\mathbf{w}_d} = \frac{\left| \sum_{k=0}^{N-1} (\mathbf{w}_d)_k \right|^2}{N \sum_{k=0}^{N-1} |(\mathbf{w}_d)_k|^2}, \quad (3.34)$$

$$\text{SNR}_{\mathbf{w}_v} = \frac{\left| \sum_{k=0}^{N-1} (\mathbf{w}_v)_k \right|^2}{N \sum_{k=0}^{N-1} |(\mathbf{w}_v)_k|^2}. \quad (3.35)$$



# Chapter 4

## 5G NR Performance Results

In this work 5G NR baseband waveforms are generated in the MATLAB environment through the help of built-in functions available in the 5G Toolbox. Simulations are carried out to evaluate the performance of the periodogram-based OFDM radar, described in Section 3.2, to compare the behaviour of NR waveforms with different characteristics and their feasibility for high-precision range and velocity estimation. In these evaluations, waveforms with subcarrier spacing (SCS)  $\Delta f = 15$  kHz and bandwidth equal to 20 MHz, and also waveforms with  $\Delta f = 30$  kHz and bandwidth equal to 40 MHz and 100 MHz, are adopted. For the generation of the symbol, a quadrature phase-shift keying (QPSK) modulation alphabet is used, with each OFDM symbol normalized to have unitary power. A downlink radio frame of 10 ms is transmitted for each simulation. The main OFDM radar parameters are summarized in Table 4.1.

	NR 20	NR 40	NR 100
Passband width (MHz)	19.08	38.16	98.28
Subcarrier spacing $\Delta f$ (kHz)	15	30	30
Cyclic prefix length ( $\mu s$ )	4.7	2.3	2.3
IFFT length	2048	4096	4096
Active subcarriers	1272	1272	3276
OFDM symbols	140	280	280

Table 4.1: OFDM Radar parameters for the considered NR channel bandwidths

The assumed carrier frequency is  $f_c = 3.5$  GHz, therefore, according to  $\Delta r$  and  $\Delta v$  in (3.18) and (3.19) respectively, the resolution in the range-Doppler map can be calculated, as shown in Table 4.2. The main downlink physical

channels and signals, such as CSI-RS, SS burst, CORESET, PT-RS, PDSCH and PDCCH, are modeled when applicable. A basic rectangular window, shown in Section 3.2.5, is used as the window function  $(\mathbf{W})_{k,l}$  in (3.30).

In order to study the performance of this signal, a simple radar system, which generates the received signal  $b_y(t)$  of (3.1), has been developed. The distance from the radar,  $r$ , and the relative velocity,  $v_{\text{rel}}$ , of a target are chosen and according to these values the generated baseband waveform is attenuated by a factor  $a$ , delayed by a value  $\tau$  and a Doppler frequency  $f_D$  is applied, according to the equations (3.2), (3.3) and (3.4) respectively. Then, as a first approximation, complex white Gaussian noise of variance  $N_0$  is added to the signal.

	NR 20	NR 40	NR 100
Distance resolution $\Delta d$ (m)	7.9	3.9	1.5
Maximum distance $d_{\text{max}}$ (m)	700	350	350
Velocity resolution $\Delta v$ (m/s)	4.2	4.2	4.2
Maximum velocity $v_{\text{max}}$ (m/s)	$\pm 64$	$\pm 128$	$\pm 128$

Table 4.2: Key parameters for the considered NR channel bandwidths at 3.5GHz

## 4.1 Range-Doppler Image

The main goal of Section 3.2 was to present an algorithm for radar detection. Therefore, the resulting matrix,  $\mathbf{Per}$ , expressed in (3.14) has been computed to create the range-Doppler map, which aims to simultaneously show the estimated range and radial velocity of the target. This map is a graphic representation of the matrix  $\mathbf{Per}$ .

In this section, in order to show a radar image similar to those generally obtained through radar signals, such as FMCW, the axes have been converted from bin indices to range and Doppler values. The abscissa represents the range in the interval  $[0; r_{\text{max}}]$ , whereas the ordinate represents the radial velocity in the interval  $[-v_{\text{max}}; v_{\text{max}}]$ , where for negative velocity the target moves towards the base station.

Figure 4.1 shows an example of a range-Doppler map where a 5G downlink signal of duration 10 ms, SCS = 30 kHz and BW = 40 MHz is transmitted. The dimensions of the image correspond to the values in Table 4.2, but to obtain a map with a better definition, the resolution is further improved choosing values of  $n$  and  $m$ , shown in (3.17), with a step  $\ll 1$ . The colour

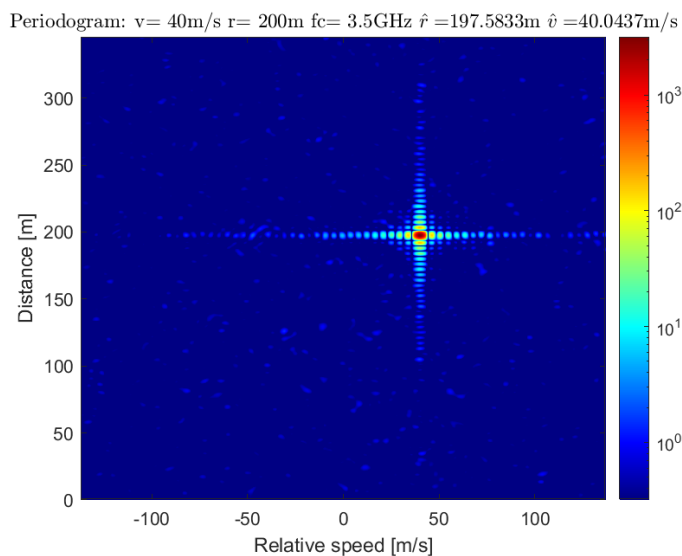


Figure 4.1: Example of a Range-Doppler image obtained through periodogram calculation when a single target is present at 200 m with a relative speed of 40 m/s in AWGN channel. The signal is characterized by SCS = 30 kHz and BW = 40 MHz.

of the periodogram's bins are related to the power received from the target, represented as a red spot due to a higher intensity. Nevertheless, since in this case AWGN noise is considered, the image presents impurities, which become more and more pronounced as the noise level increases. It can be noticed that, unless the noise overwhelms the signal, the correctness of the algorithm is confirmed.

As seen in Section 3.2.5, the main advantage of a window function is to enable a finer control of sidelobe levels, useful especially for a reliable detection of multiple targets. Figure 4.2 shows the range-Doppler map for two identical cases, but each using a different window. The periodogram is evaluated when three targets are present, in particular two targets have the same distance from the radar and the same radial velocity, but one target moves away from the receiver whereas the other moves towards it. Another target is present at a higher distance, but is characterized by a lower RCS therefore reflects less power. In the first case, a rectangular window is used, hence the main lobe width is very small and targets close to each other can be distinguished, but there is less sidelobe attenuation. In the second case, a Dolph-Chebyshev window is applied, which is characterized by a higher sidelobe attenuation. This allows weaker targets to be better distinguished

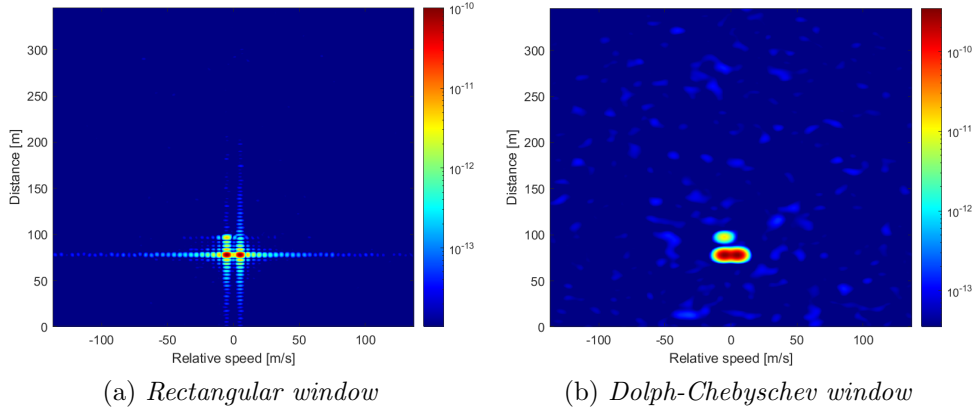


Figure 4.2: Periodogram of multiple targets obtained with a different window choice in AWGN channel. The downlink signal is characterized by SCS = 30 kHz and BW = 40 MHz.

from sidelobes of stronger targets, but reduces the radar resolution, hence targets close to each other are not easily distinguished.

## 4.2 Performance in AWGN Channel

In this section, the performance of the radar system implemented, in terms of root mean square error (RMSE) of the distance and velocity estimation, is studied for AWGN channel. At first, the 5G waveform generated needs to be normalized in order to verify the assumption (5) in Section 3.2.3. The actual number of subcarriers of the signal is given by the number of points of the IFFT at the modulator,  $N_{\text{IFFT}}$ , but only a number  $N < N_{\text{IFFT}}$  are active and actually used in the transmitted frame matrix. Therefore the power after the IFFT block needs to be normalized to unit power according to the following expression:

$$P_{x_{norm}} = \frac{N_{\text{IFFT}}^2}{N} P_x \quad (4.1)$$

where  $P_x$  is the transmitted power after the IFFT block, and  $P_{x_{norm}}$  is the normalized transmitted power.

Hence, the transmitted waveform is normalized to unit power as follows:

$$\mathbf{b}_{x_{norm}} = \frac{N_{\text{IFFT}}}{\sqrt{N}} \mathbf{b}_x. \quad (4.2)$$

This is necessary because the IFFT introduces a power loss due to the inactive subcarriers and of the multiplicative factor,  $N$ , appearing in its definition.

Now, taking into account the presence of the inactive subcarriers, the parameter  $E_s/N_0$ , which represents the symbol energy to noise power spectral density ratio, can be written as:

$$\frac{E_s}{N_0} = \frac{E_b}{N_0} \frac{Nk}{N_{\text{IFFT}}} \quad (4.3)$$

where  $E_s$  is the energy per symbol,  $N_0$  is the noise spectral density,  $E_b$  is the energy per bit, and  $k$  is the number of bits per symbol (in this case equal to 2, because a QPSK modulation has been used). Considering the equation (4.3), the SNR in linear scale can be calculated as:

$$\text{SNR}_{\text{lin}} = \frac{E_s f_s}{N_0 \text{BW}} \quad (4.4)$$

where  $f_s$  is the sampling frequency,  $E_s f_s$  is the power of the signal and BW is the bandwidth of the signal. According to the assumption (5) and the normalization applied in (4.2), the energy per symbol can be assumed  $E_s = 1$ .

### 4.2.1 Numerical Performance Analysis

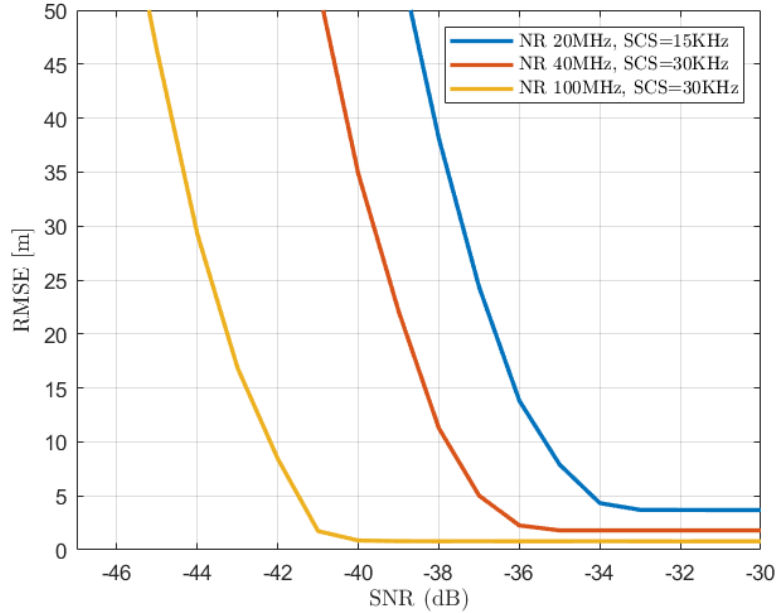
In these simulations, the main goal is to analyze the performance for different values of the SNR at the receiver. It was chosen to define a set of SNR[dB] values and derive the noise spectral density  $N_0$  from the equation (4.4) to define the noise samples to add to the signal. So, in this case, it has been chosen to vary the SNR through  $N_0$  while keeping constant the power of the received signal at varying the target's distance.

At first, the SNR is transformed from dB to the linear scale through  $\text{SNR}_{\text{lin}} = 10^{(-\text{SNR}[\text{dB}]/10)}$ , to obtain:

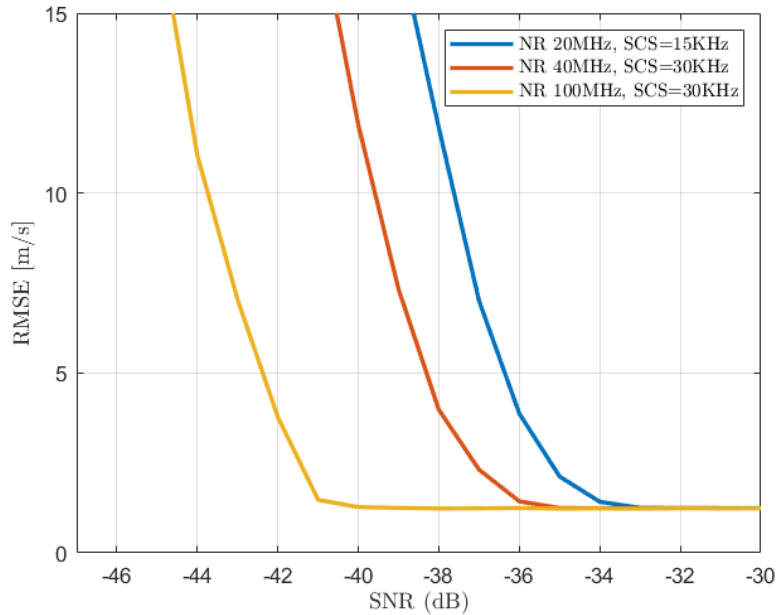
$$N_0 = \frac{f_s}{\text{SNR}_{\text{lin}} \cdot \text{BW}}. \quad (4.5)$$

The evaluations are carried out when only a single target is present. The actual distance and velocity of the target is varied randomly, through  $M$  Monte Carlo iterations, with uniform distributions from 20 to 200 m (distance) and from  $-40$  to  $40$  m/s (velocity). In each iteration, the signal is delayed by a quantity  $\tau$  and a Doppler frequency  $f_D$  is applied. In the radar processing, no prior information about the target distance or speed is assumed, therefore, in the periodogram calculations and the corresponding detector, the overall feasible space contains distances up of a one-way propagation delay and velocities up to the maximum velocity detectable  $v_{\text{max}}$ . The resolution of the periodogram is chosen according to the parameters of Table 4.2.

---



(a) target distance estimation RMSE



(b) target velocity estimation RMSE

Figure 4.3: Radar performance at 3.5 GHz as a function of the SNR at the receiver input when a single target is present.

As shown in Figure 4.3, the RMSE is calculated, which is a measure of absolute error in which errors are squared to prevent positive and negative values from canceling each other out. The expression of the RMSE can be written as follows:

$$\text{RMSE} = \sqrt{\frac{1}{K} \sum_{k=1}^K (\hat{x}_k - x_k)^2} \quad (4.6)$$

where  $x$  is the parameter for which the RMSE needs to be calculated, in this case the actual distance from the radar and the relative velocity of the target, whereas  $\hat{x}$  is the estimation of this parameter.

As can be seen, reliable target detection can be achieved for input SNRs in the order of -33 to -41 dB, the exact number depending on the channel bandwidth and subcarrier spacing. At these SNR values the distance and velocity estimation errors are coherent with the resolution values of the radar shown in Table 4.2. The RMSE values converge toward  $\sqrt{(\Delta r)^2/12}$  and  $\sqrt{(\Delta v)^2/12}$  for distance and velocity, respectively, reflecting uniform error distribution within the pixel width as in [13].

## 4.3 Performance in Multipath Fading Channel

Generally, radio propagation channels can be classified into: line-of-sight (LOS) and non-line-of-sight (NLOS). In the first case, signals travel through the wireless medium mainly in a direct path without encountering any obstacles from a transmitter to a receiver. In the latter case, signals from the transmitter encounter multiple obstacles before arriving at the receiver, therefore the line of sight is obstructed. In both scenarios, signals can be reflected, scattered, diffracted, refracted or absorbed by obstacles i.e. buildings, trees, ground, creating a multipath propagation. Therefore different versions of the signal arrive at the receiver at different times, from different paths, and with different power.

### 4.3.1 Channel Characterization

Generally, for a communication channel, the main parameters which describe the behaviour of the channel in the presence of multipath propagation are: Power Delay Profile, RMS Delay Spread, and the Maximum Excess Delay.

---

### Power Delay Profile

The power delay profile describes how the power of the received signal, filtered through a multipath channel, varies as a function of the time delay, and is defined as follows

$$P_h(t) = |h(t)|^2 = \left| \sum_{l=0}^{L-1} h[l] \delta(t - \Delta t) \right|^2 \quad (4.7)$$

where  $h(t)$  is a continuous channel impulse response,  $h[l]$  is the discrete time channel impulse response,  $L$  is the number of samples and  $\Delta t$  is the size of the time step.

In a power delay profile plot, the signal power of each path is plotted against their respective propagation delays.

### RMS Delay Spread

The mean delay spread ( $\tau_{\text{mean}}$ ) is the statistical mean of the delay introduced by the multipath channel when a signal is transmitted. For a discrete channel it is given by:

$$\tau_{\text{mean}} = \langle \tau \rangle = \frac{\sum P_h(\tau) \tau}{\sum P_h(\tau)}. \quad (4.8)$$

RMS delay spread, denoted as  $\tau_{\text{rms}}$ , is similar to the standard deviation of a statistical distribution. For a discrete channel it is calculated as follows:

$$\langle \tau^2 \rangle = \frac{\sum P_h(\tau) \tau^2}{\sum P_h(\tau)}. \quad (4.9)$$

$$\tau_{\text{rms}} = \sqrt{\langle \tau^2 \rangle - \langle \tau \rangle^2}. \quad (4.10)$$

The RMS delay spread is inversely proportional to the coherence bandwidth  $B_c$ , which is the bandwidth over which a channel may be considered flat. To avoid ICI, it is important that the subcarrier spacing is chosen larger than the Doppler spread. However, to make sure that adjacent carriers from one OFDM symbol experience similar fading coefficients,  $\Delta f$  must also be smaller than the coherence bandwidth of the channel:

$$B_D \ll \Delta f \ll B_c \quad (4.11)$$

where  $B_D$  is the Doppler spread, which describes the widening of the spectrum caused by different Doppler shifts on each multipath. It is inversely proportional to the coherence time  $T_C$ , which is the time over which the channel may be assumed constant.

---

### Maximum Excess Delay

Maximum excess delay  $\tau_e$  is the relative time difference between the first signal arriving at the receiver and the last signal whose power level is above a given threshold. If the maximum excess delay is greater than the symbol time period, the ISI arises and the signal is distorted, therefore another condition must be verified

$$T_1 > \tau_e. \quad (4.12)$$

### 4.3.2 Numerical Results

The evaluations in this section are carried out in the same way as for the AWGN channel. In particular, the transmitted signal is normalized to unit power according to (4.2). A single target is considered, and the actual distance and velocity of the target is varied randomly with uniform distributions from 20 to 200 m (distance) and from  $-40$  to  $40$  m/s (velocity). In each iteration, the signal is delayed by a quantity  $\tau$  and a Doppler frequency  $f_D$  is applied. As for the AWGN channel, the signal is not attenuated by a factor  $a_h$ , contrary to the expression given in (3.1). Furthermore, the signal is filtered through a multipath fading channel with the characteristic summarized in Table 4.3. For the radar case, if shadowing is not considered, as in this case, a main path is present and the multipath fading channel is characterized by a Rician distribution i.e., the direct path follows a Rice distribution, while the diffuse component is modeled with a Rayleigh one. In this evaluation a simple power delay profile of a two-ray model is considered, where the first ray (which models a bundle of rays with similar delays) is the direct component and has an average path gain of 0 dB, whereas the second ray (which also models a bundle of rays with similar delays) consists of multipath components with an average path gain (APG) and path delay given in Table 4.3.

Fading distribution	Rician
K Factor (direct path)	100
RMS Delay spread	130 ns
Average Paths gain (APG)	-15dB

Table 4.3: Parameters of the multipath fading channel

These additional paths are regarded as interference, therefore the SNR has to be expressed in another form. At first, in order to estimate the attenuation introduced by the channel, a discrete pilot tone  $d[k]$ , which consists of a Dirac

---

impulse, is transmitted and filtered by the channel. The attenuation  $\alpha$  is the response of the channel to this signal and can be expressed as follows:

$$\alpha = |d[1]|^2. \quad (4.13)$$

This attenuation is considered only for the direct reflected signal, whereas for the interference introduced by the multipath components another notation must be introduced, called signal to interference ratio (SIR). This parameter is defined as the ratio between the power of the signal and the total power  $I$  of the interference signals, which are signals that fall in the same bandwidth of the signal transmitted but are not useful. The SIR is obtained through the average paths gain of the second ray, which correspond to the power of the interference signal with respect to the useful signal, as  $\text{SIR}[\text{dB}] = -\text{APG}[\text{dB}]$  and can be easily transformed to the linear scale  $\text{SIR}_{\text{lin}} = 10^{(-\text{APG}[\text{dB}]/10)}$ . The SNR in the case of multipath fading channel in linear scale becomes:

$$\text{SNR}_{\text{lin}} = \frac{\alpha E_s f_s}{N_0 BW} \left( 1 + \frac{1}{\text{SIR}_{\text{lin}}} \right) \quad (4.14)$$

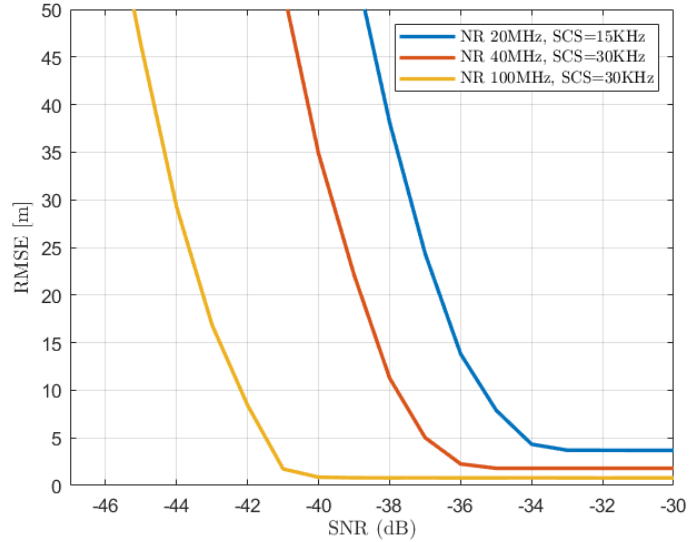
where  $E_s = 1$  for the same assumption made for the case of AWGN channel. Consequently, the noise spectral density becomes:

$$N_0 = \frac{\alpha(\text{SIR}_{\text{lin}} + 1)f_s}{\text{SNR}_{\text{lin}}\text{SIR}_{\text{lin}}BW}. \quad (4.15)$$

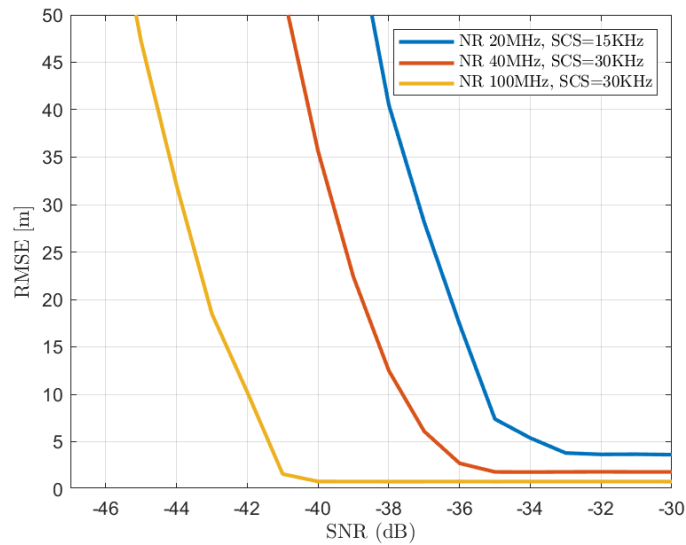
Figure 4.4 and 4.5 show a comparison between the performance of the radar system when different channels are applied to the signal. It can be seen that, due to the randomness of the fading channel, the curves are not as smooth as for the case of AWGN channel. In Figure 4.6 a better representation of the deterioration of the performance caused by interference and attenuation introduced by the channel is shown. It can be seen that when a multipath scenario is introduced, errors both in the distance and in the velocity estimation begin to increase for values of SNR higher than those of the AWGN channel. Furthermore, if the SIR decreases, the error increases at higher SNR, i.e. for  $\text{SIR} = 5$  dB where the distance estimation no longer converges towards  $\sqrt{(\Delta r)^2/12}$  as for the other cases, because the power of the multipath components is now higher and also closer to the power reflected by the true target, making distance estimation more difficult.

On the contrary, the RMSE on the velocity is not affected by the SIR as for the RMSE on the distance and, despite a degradation of the velocity estimation, the error still converges towards  $\sqrt{(\Delta v)^2/12}$ . This stems from the fact that velocity estimation for OFDM radar is performed through estimation of

---

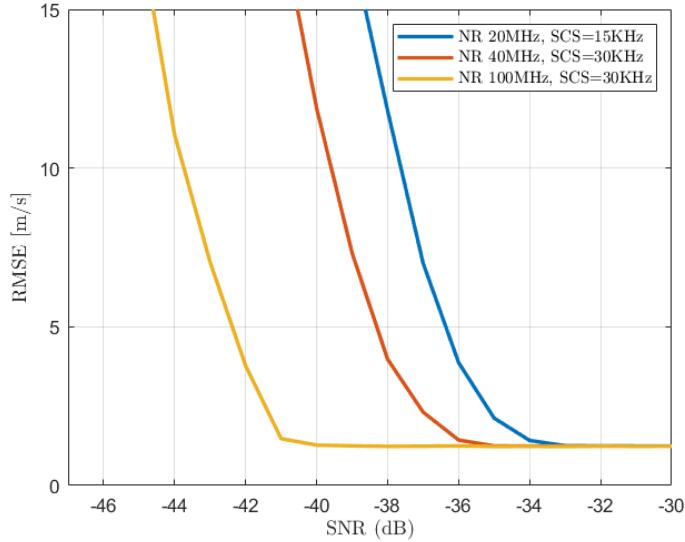


(a) target distance estimation RMSE in AWGN channel

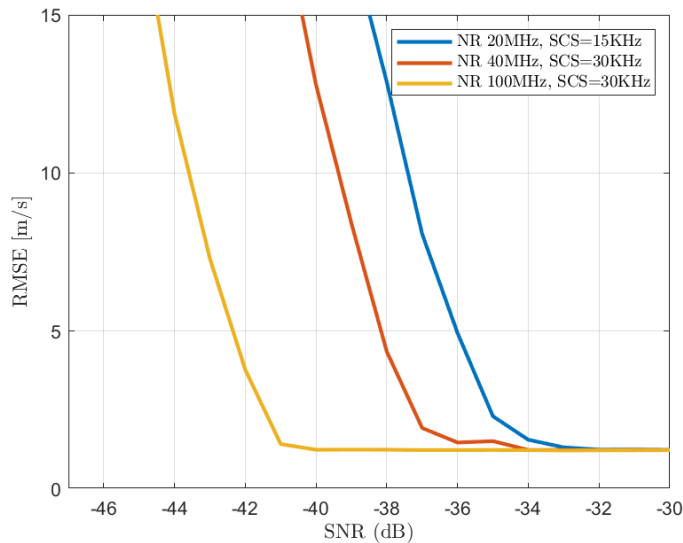


(b) target distance estimation RMSE in multipath fading channel

Figure 4.4: Radar performance at 3.5 GHz as a function of the SNR at the receiver input when a single target is present. Comparison of the distance estimation RMSE when an AWGN channel and a multipath fading channel, with a SIR = 15 dB of the multipath components relative to the direct path, is considered.

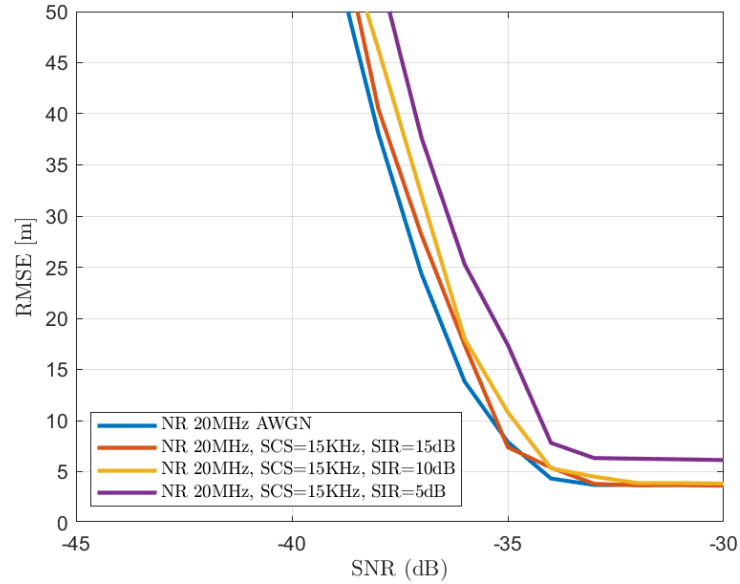


(a) target distance estimation RMSE in AWGN channel

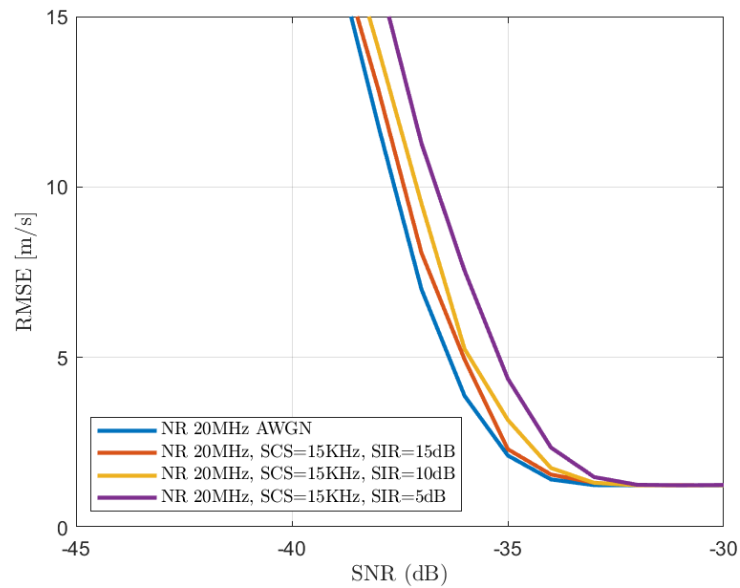


(b) target velocity estimation RMSE in multipath fading channel

Figure 4.5: Radar performance at 3.5 GHz as a function of the SNR at the receiver input when a single target is present. Comparison of the velocity estimation RMSE when an AWGN channel and a multipath fading channel, with a SIR = 15 dB of the multipath components relative to the direct path, is considered.



(a) target distance estimation RMSE



(b) target velocity estimation RMSE

Figure 4.6: Radar performance at 3.5 GHz as a function of the SNR at the receiver input when a single target is present. Comparison between AWGN channel and multipath fading channel for a downlink signal with SCS = 15 kHz and BW = 20 MHz for 3 values of SIR [5dB, 10dB, 15dB].

Doppler-induced complex exponentials, whereas distance estimation is based on the processing of delay-induced complex exponentials and therefore is more sensitive to time delays.

## 4.4 Signal Detection and False Alarm Rate

A target detector must be part of the periodogram-based OFDM radar system in order to estimate real target locations from peaks of the periodogram matrix  $\mathbf{Per}_{\bar{\mathbf{G}}}(n, m)$  and differentiate them from spurious effects. In this case, there are two main causes of errors:

- peaks caused by the AWGN;
- ambiguities caused by targets' side lobes.

Hence, two types of detection errors can arise from this:

1. Missed target: a valid target can be missed because it is identified as a side lobe of another, previously detected, target with higher backscattered power;
2. False alarm: a side lobe of a previously detected target can be identified as the main lobe of a non-existent target.

As mentioned previously, the choice of a suitable window matrix  $W$  can decrease the ambiguities caused by targets' sidelobes since they can be controlled, at the cost of reduced resolution. However, peaks caused by AWGN are still a source of error.

In order to evaluate the performance of the detector, ROC curves are used. They consist of a graphical plot that illustrates the diagnostic ability of a system varying the discrimination threshold  $\eta$ , for constant SNR. This plot is derived through a diagnostic test which consists of subjecting the periodogram to a hypothesis test:

$$\mathbf{Per}_{\bar{\mathbf{G}}}(n, m) \underset{H_0}{\overset{H_1}{\gtrless}} \eta \quad (4.16)$$

where  $H_0$  is the null hypothesis (no target is present) and  $H_1$  is the hypothesis that a target contributes to the amplitude of the given bin. The location of the peak of the periodogram can be obtained through the maximum likelihood estimator:

---

$$(\hat{n}, \hat{m}) = \underset{(n,m)}{\operatorname{argmax}} \quad \mathbf{Per}(n, m). \quad (4.17)$$

The ROC curve plot shows the *true positive rate* against the *false positive rate* at various threshold values.

- *True positive rate* (TPR), also known as sensitivity or probability of detection, is defined as the probability of detecting a target when it is indeed present. It is expressed as follows:

$$\text{TPR} = \frac{\text{TP}}{\text{P}} \quad (4.18)$$

where TP represents the true positive, or number of times a real target is detected, whereas P is the number of real positive cases. Therefore (4.18) is defined as the number of correct positive results occurring among all positive samples available during the test.

- *False positive rate* (TFR), also known as probability of false alarm, defined as the event where the target detector decides that there is a target at a range and relative speed which did not contribute to the received matrix  $\bar{\mathbf{G}}_{\text{Rx}}$ , but only noise was present ( $\bar{\mathbf{G}}_{\text{Rx}} = \mathbf{Z}$ ). It is expressed as follows:

$$\text{FPR} = \frac{\text{FP}}{\text{N}} \quad (4.19)$$

where FP represents the false positive, or number of times a target is detected when only noise is received by the radar, whereas N is the number of real negative cases. Therefore, (4.19) is defined as the number of incorrect positive results occurring among all negative samples available during the test.

The main advantage of this plot stems from the value of the area under the curve, which represents the accuracy of the test. The greater the area under the curve, the more accurate the test. The best possible prediction method corresponds to a step function, representing no false negatives and no false positive. A random guess, such as a flip of a coin, is represented by a diagonal line in the plot, which also divides the ROC space. Points above the diagonal line represent good classification results, whereas points below such line represent bad results.

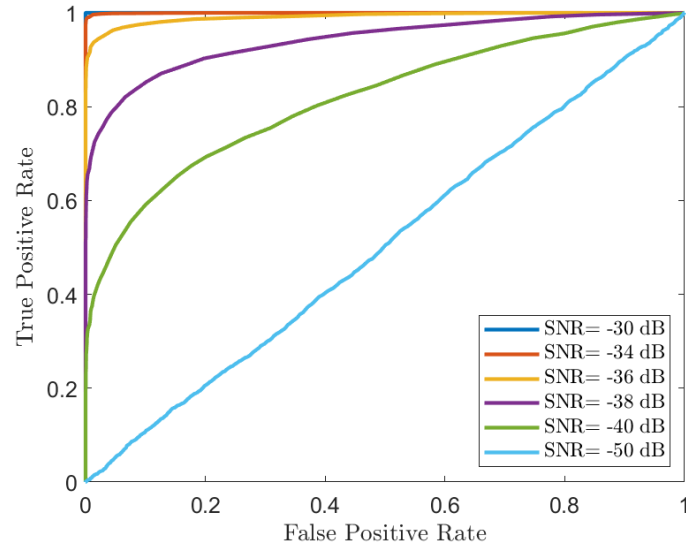
In order to calculate the expressions mentioned previously in this section, the periodogram needs to be calculated. For this case the simulations are similar to those performed in the previous sections for different values of SNR, but during each Monte Carlo iteration a decision is made whether the

---

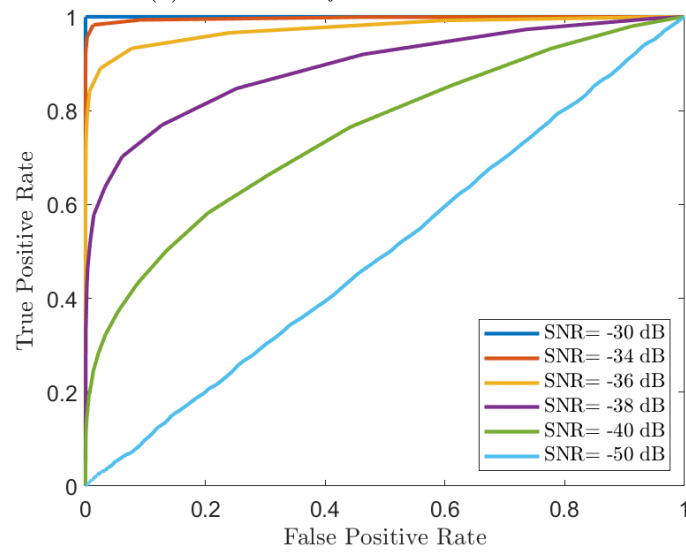
signal should be transmitted or if only noise is present and consequently the value of  $N$  and  $P$  can be calculated. Once the periodogram is calculated, it undergoes the threshold test in order to decide if the target is present or not and the values  $TP$  and  $FP$  can be calculated.

In Figure 4.7, 4.8 and 4.9 the ROC curves for the various bandwidth taken into consideration are shown. For all cases under investigation, the detector performance has been analyzed both in presence of a simple AWGN channel and a multipath fading channel with the same characteristics shown in Table 4.3. As it can be seen, as the bandwidth increases, the curves tend towards the step function for low values of SNR. For the signal with  $BW = 100$  MHz at  $SNR = -40$  dB the curve resembles the step function whereas for signals with  $BW = 20$  MHz at  $SNR = -38$  dB the curve is already degraded. This is verified by the curves shown in Figure 4.3 where it can be seen that target detection errors start to increase sooner for shorter bandwidth. Furthermore, for every case, a visible degradation of the curve between the scenario of a simple AWGN channel and the fading channel is shown as the bandwidth increases.

---

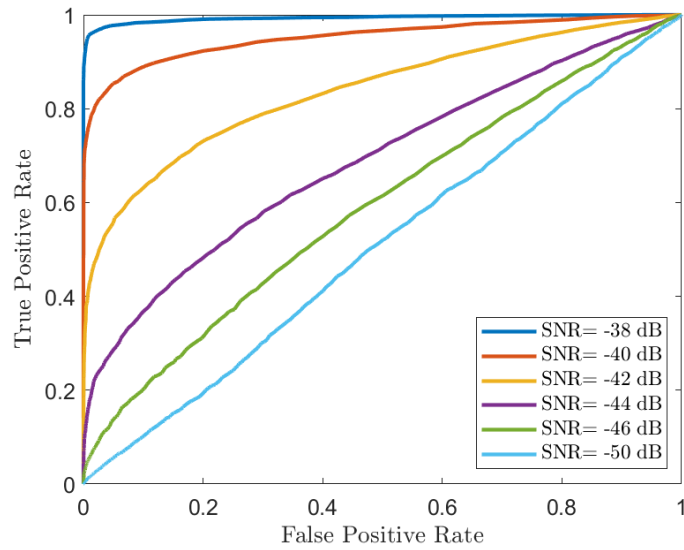


(a) ROC curve for AWGN channel



(b) ROC curve for multipath fading channel with SIR = 15 dB

Figure 4.7: Comparison between ROC curves for different channels when a 5G NR signal with SCS = 15 kHz and BW = 20 MHz is transmitted.



(a) ROC curve for AWGN channel

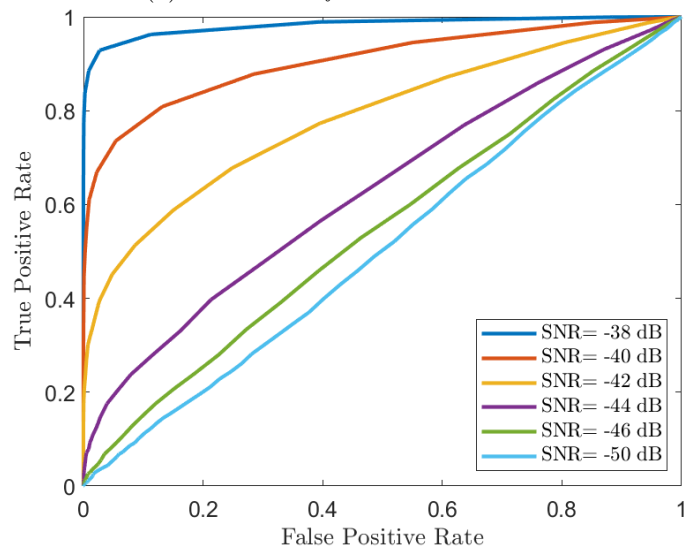
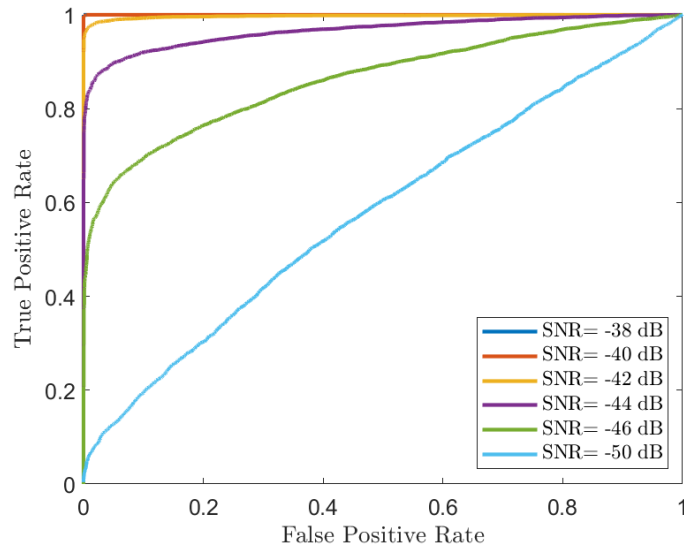
(b) ROC curve for multipath fading channel with  $SIR = 15$  dB

Figure 4.8: Comparison between ROC curves for different channels when a 5G NR signal with SCS = 30 kHz and BW = 40 MHz is transmitted.



(a) ROC curve for AWGN channel

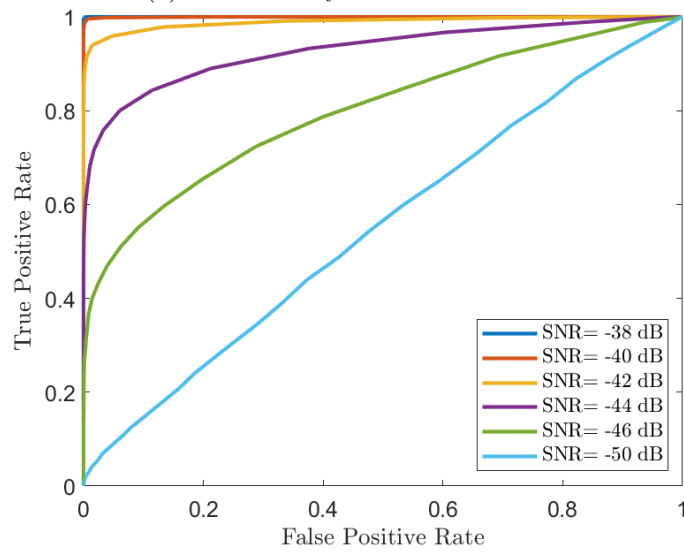
(b) ROC curve for multipath fading channel with  $SIR = 15dB$ 

Figure 4.9: Comparison between ROC curves for different channels when a 5G NR signal with SCS = 30 kHz and BW = 100 MHz is transmitted.



# Conclusions

The purpose of this thesis was to introduce the 5G NR technology along with its application to radar systems, and to show the main performance results. At first, the general OFDM system model was analyzed, in order to understand the main characteristics of the 5G signal, which consists of an OFDM signal after all. Then, a classical frequency domain OFDM radar processing approach was studied, complemented with an interpolation method to account for null subcarriers within the transmit resource grid, in order to study the performance of the radar system varying the SNR at the receiver. Two types of channels have been considered, a simple AWGN channel and a multipath fading channel.

In this thesis three different 5G waveforms were targeted, therefore the analysis was carried out varying two main parameters: the number of active subcarriers  $N$  (which is strictly correlated with the bandwidth) and the number  $M$  of OFDM symbols (which depends on the SCS).

At first, a basic monostatic radar system was designed, then the different types of 5G waveforms were generated and used in order to verify the correctness of the signal processing algorithm devised for an OFDM radar system. Subsequently, simulations were carried out, in which the position and the velocity of the target were estimated. A first analysis was focused on the RMSE between the actual position and velocity of the target, and the parameters estimated by the periodogram-based algorithm. A second type of simulations was focused on the performance of the detector through the analysis of ROC curves, obtained performing a binary test.

In Chapter 4 it has been shown that if the number of subcarriers increases, the distance resolution is improved, whereas the velocity resolution mainly depends on the carrier frequency  $f_c$ . Furthermore, from the results shown in Figure 4.3, it can be seen that, for higher bandwidth, target detection remains reliable for values of SNR lower than the case for smaller bandwidth. In Figure 4.6, results obtained from the two types of channel considered are shown, in order to compare the behaviour of the radar processing algorithm when only noise is present and when the channel also presents multipath

propagation. The implemented multipath channel model features two paths, where each path models a cluster of paths with similar delays; the first path is the direct one, while the second one is regarded as interference. When the interference power increases, a degradation of the detection algorithm occurs, mainly caused by different paths which arrive at the receiver with different delays and different powers that can dominate the true target path. This can be seen clearly from the ROC curves produced for both channels.

The results obtained in this thesis, together with other cited results available in the scientific literature, suggest that 5G NR waveforms are a viable option to perform radar applications, and can compete with the more traditional radar waveforms. An important next step would be the performance analysis of a dual-function radar and communication system, and also the extension of the analysis in this work, based on a single transmitting and receiving antenna, to a MIMO framework. 5G NR networks, in order to achieve better spectral efficiency, aim to work with hybrid massive MIMO, designed for communication purposes, where the number of antennas at the base station is much larger than the number of devices and hybrid beamforming is used, which combines multiple array elements into subarray modules, with one transmit/receive module dedicated to a subarray in the array.

---

# List of Figures

1.1	Block diagram of the OFDM modulation stages [2]. . . . .	4
1.2	Cyclic extension and windowing for three OFDM subcarriers [2]. . . . .	7
1.3	Spectrum of an OFDM signal [5]. . . . .	8
1.4	Comparison between OFDM spectra using two different values for the window that defines the FFT interval. (a) using $T_p=T$ results in orthogonality, (b) using $T_p > T$ the subcarriers are no longer orthogonal [2]. . . . .	9
1.5	Transmission stages including oversampling [2]. . . . .	11
1.6	Time-frequency representation of the OFDM radar signal: $\mu$ is the index of the OFDM symbol whereas $N_{sym}$ is the number of OFDM symbols [5]. . . . .	12
2.1	Frequency ranges FR1 and FR2 and corresponding IMT identifications. Note that the frequency scales are logarithmic [7].	18
2.2	Frame, subframes and slots in NR [7]. . . . .	20
2.3	Handling of the DC subcarrier in LTE and NR [7]. . . . .	21
2.4	Resource grid and resource element in 5G [7]. . . . .	21
2.5	Example of bandwidth adaptation using bandwidth parts [7].	23
3.1	Schematic of a radar system [9]. . . . .	26
3.2	Block diagram of a periodogram-based OFDM radar system [10]. . . . .	32
4.1	Example of a Range-Doppler image obtained through periodogram calculation when a single target is present at 200 m with a relative speed of 40 m/s in AWGN channel. The signal is characterized by SCS = 30 kHz and BW = 40 MHz. . . . .	41
4.2	Periodogram of multiple targets obtained with a different window choice in AWGN channel. The downlink signal is characterized by SCS = 30 kHz and BW = 40 MHz. . . . .	42

---

4.3	Radar performance at 3.5 GHz as a function of the SNR at the receiver input when a single target is present. . . . .	44
4.4	Radar performance at 3.5 GHz as a function of the SNR at the receiver input when a single target is present. Comparison of the distance estimation RMSE when an AWGN channel and a multipath fading channel, with a SIR = 15 dB of the multipath components relative to the direct path, is considered. . . . .	49
4.5	Radar performance at 3.5 GHz as a function of the SNR at the receiver input when a single target is present. Comparison of the velocity estimation RMSE when an AWGN channel and a multipath fading channel, with a SIR = 15 dB of the multipath components relative to the direct path, is considered. . . . .	50
4.6	Radar performance at 3.5 GHz as a function of the SNR at the receiver input when a single target is present. Comparison between AWGN channel and multipath fading channel for a downlink signal with SCS = 15 kHz and BW = 20 MHz for 3 values of SIR [5dB, 10dB, 15dB]. . . . .	51
4.7	Comparison between ROC curves for different channels when a 5G NR signal with SCS = 15 kHz and BW = 20 MHz is transmitted. . . . .	55
4.8	Comparison between ROC curves for different channels when a 5G NR signal with SCS = 30 kHz and BW = 40 MHz is transmitted. . . . .	56
4.9	Comparison between ROC curves for different channels when a 5G NR signal with SCS = 30 kHz and BW = 100 MHz is transmitted. . . . .	57

---

# Bibliography

- [1] F. Liu, C. Masouros, A. Petropulu, H. Griffiths, and L. Hanzo, “Joint Radar and Communication Design: Applications, State-of-the-art, and the Road Ahead”, *IEEE Transactions on Communications*, Feb. 2020.
- [2] Durney Wasaff, Hugo Ivan, “Adaptive pre-distortion for nonlinear high power amplifiers in OFDM systems”, Tesi doctoral, UPC, Departament de teoria del Senyal i Comunicacions, July 2004.
- [3] R. Van Nee and R. Prasad: *OFDM for Wireless Multimedia Communications*, Artech House, pp.39-42, 2000.
- [4] Bhad, Sandeep, Pankaj Gulhane, and A. S. Hiwale, “PAPR reduction scheme for OFDM.” *Procedia Technology*, vol. 4, pp. 109-113, 2012.
- [5] Hakobyan, Gor, “Orthogonal Frequency Division Multiplexing Multiple-Input Multiple-Output Automotive Radar with Novel Signal Processing Algorithms”, 2018
- [6] Series, M. “IMT Vision - Framework and overall objectives of the future development of IMT for 2020 and beyond”, *Recommendation ITU-R*, M.2083-0, Sept. 2015.
- [7] Dahlman, Erik, Stefan Parkvall, and Johan Skold, “5G NR: The Next Generation Wireless Access technology”, Academic Press, 2018.
- [8] 3GPP Technical Specifications Group RAN: TS 38.211 (Release 15): Physical channels and modulation, July 2018.
- [9] K. M. Braun, “OFDM radar algorithms in mobile communication networks”, Ph.D. dissertation, Karlsruhe Inst. Technol., Karlsruhe, Germany, 2014.
- [10] Zhang, H., Zhang, Y., Qi, X., and Zong, C., “Moving target detection based on OFDM radar”, *The Journal of Engineering*, Vol. 2019, Issue 19, pp. 5605-5609, May 2019.

- [11] C. Sturm and W. Wiesbeck, “Waveform design and signal processing aspects for fusion of wireless communications and radar sensing”, *Proceedings of the IEEE*, vol. 99, no. 7, pp. 1236–1259, July 2011.
- [12] M. Braun, C. Sturm, and F. K. Jondral, “Maximum likelihood speed and distance estimation for OFDM radar”, *IEEE Radar Conference*, pp. 256–261, May 2010.
- [13] C.B. Barneto, T. Riihonen, M. Turunen, L. Anttila, M. Fleischer, K. Stadius, J. Ryyanen, and M. Valkama, “Full-Duplex OFDM Radar With LTE and 5G NR Waveforms: Challenges, Solutions, and Measurements”, *IEEE Transactions on Microwave Theory and Techniques*, vol. 67, no. 10, pp. 4042–4054, Oct. 2019.
- [14] M. A. Richards, W. A. Holm, and J. A. Scheer, “Principles of Modern Radar: Basic Principles”. London, U.K.: IET, 2010.
- [15] Harris, Fredric J,: “On the Use of Windows for Harmonic Analysis with the Discrete Fourier Transform”, *Proceedings of the IEEE*, vol. 66, no. 1, pp. 51-83, 1978.